Journal of Inorganic and Organometallic Polymers and Materials
https://doi.org/10.1007/s10904-024-03405-9

RESEARCH

Optoelectronic and Thermoelectric Properties of Zirconium Half-Heusler Alloys RhZrX (X = P, As, Sb, Bi): an *ab-initio* Investigation

Mumtaz Manzoor[1] · Arti Saxena[2] · Pramod Kumar Singh[3] · Faizan Ahmad[1] · Ramesh Sharma[4] · Hamid Ullah[5] · Dalia Fouad[6] · Vipul Srivastava[7]

Received: 11 July 2024 / Accepted: 8 September 2024

Abstract
A full potential linearized augmented plane-wave (FP-LAPW) method based on density functional theory (DFT) was employed using various approximations to provide insight into the novel half-Heusler (HH) RhZrX (X = P, As, Sb, Bi) alloys. The total energy calculations determine materials' stability in F-43 m structure. Trans-Blaha modified Beck Johansen (TB-mBJ) potential has been used successfully to address the issue of different band gaps in the materials. According to the electronic band structure calculations using TB-mBJ, semiconducting nature with estimated indirect band gap of 1.50 eV, 1.47 eV, 1.38 eV, and 1.18 eV in RhZrX (X = P, As, Sb, Bi) alloys, respectively, has been estimated. The RhZrX (X = P, As, Sb, Bi) HH alloys are possible candidate materials for optoelectronics applications due to their absorption in the visible and UV region. Further, for these HHs, the investigated values of static dielectric constants, $\varepsilon_1(0)$ are reported to 16.40, 16.81, 16.97, 17.64, respectively, which obey Penn model. Semi-classical Boltzmann theory has been utilized to examine how temperature and chemical potential affect the Seebeck coefficient, electronic conductivity, electronic thermal conductivity, power factor, and Fig. of merit—all of which are significant factors to take into account when assessing a material's thermoelectric performances. The calculated low value of k_l (0.584 W/mKs) for RhZrAs is particularly encouraging for utilization in thermoelectric devices. Furthermore, these materials exhibit dynamical and mechanical stabilities.

Keywords Heusler alloys · DFT · Mechanical properties · Electronic properties · Vibrational properties · Lattice thermal conductivity · Fig. of merit

1 Introduction

Husler alloys have recently generated a great deal of attention in the scientific community of their amazing solar optoelectronic and thermal features [1, 2], which include tunable bandgap, strong optical absorption, a wide absorption spectrum, small effective masses of carriers, and a dominating point, high charge carrier mobility, and extended charge diffusion lengths. Nowadays, renewable energy sources are being used including solar panels [3], wind turbines [4], and hydroelectric facilities [5], to replace the worldwide reliance on non-renewable fossil fuels in the power industry. Although significant changes are occurring in primary energy production, it is crucial to focus on increasing

✉ Ramesh Sharma
sharmadft@gmail.com

✉ Vipul Srivastava
vipsri27@gmail.com

[1] Institute of Physics, Slovak Academy of Sciences, 84511 Bratislava, Slovakia

[2] Department of Electronics and Communication, Pranveer Singh Institute of Technology, Kanpur, Uttar Pradesh 209305, India

[3] Department of Applied Sciences, School of Management Sciences, Lucknow, Uttar Pradesh, India

[4] Department of Applied Science, Feroze Gandhi Institute of Engineering and Technology, Raebareli, Uttar Pradesh 229001, India

[5] Department of Physics, Riphah International University, Lahore, Pakistan

[6] Department of Zoology, College of Science, King Saud University, PO Box 22452, 11495 Riyadh, Saudi Arabia

[7] Deptartment of Physics, School of Chemical and Physical Sciences, Lovely Professional University, Phagwara, Punjab 144411, India

Published online: 22 September 2024

the whole effectiveness of global power generation [6, 7]. This can be done by enhancing electricity transmission [8], enhancing device performance [9], and restoring waste heat [10]. Waste heat may be transformed into electricity using thermoelectric generators (TEGs) [11, 12], which switch temperature gradients into electrical currents. The amount of energy that main producers would need to produce could decrease as TEGs became more widely used. When construction is a challenge or a prolonged lifespan is compulsory, TEGs can also be employed as the main generator. TEGs have a variety of operating temperatures because of their fundamental solid characteristics. Such as, the exclusively commerce-oriented TEGs relied on Bi_2Te_3 to work well between 300 and 500 K, however as the temperature rises, their efficiency starts to decrease. Novel materials are needed for the applications involving high temperatures, such as the Mars Perseverance rover's PbTe and GeTe. On the other hand, affordability and chemical richness are important extra factors for large-scale commercial applications. Further considerations include physical qualities, excellent thermal stability, matching n-type and p-type mixtures, and the efficiency of both electrical and thermal contacting within the TEG gadget. The scalability of materials' processing is another important consideration. Currently, developments involve the emergence of p-type compositions with the Fig. of merit (ZT) > 1 at 773 K, such as XVFeSb (XV = V, Nb, and Ta) and ZrCoBi [13]. It includes not only first-principles calculations [14], but also the widely-used single parabolic band (SPB) and Callaway modelling [15, 16], which have greatly improved our understanding of HH alloys [17]. The key recent advancements will be discussed in this paper, and it will wrap up with a quick summary of the growingly popular integration of HH materials into functional TEGs [18].

The HH alloys met most of these goal standards among all examined solid thermoelectric compounds. They are just constrained in terms of whole performance by extremely high lattice thermal conductivities that lower the efficiency of conversion of heat to electricity. They are well suited for power production applications regarding their electrical qualities [19]. HH alloys have drawn a lot of interest as possible thermoelectric solids due to their planned technical characteristics and TE efficiency [20, 21]. HH alloys have been considered extensively as potential transport solids [22, 23]. In the late 1990s, first study on these solids began, and the most encouraging mixtures were n-type and p-type phases that relied on XIVNiSn and XIVCoSb (XIV = Ti, Zr, and Hf) [24]. Skutterudites and tellurides, in particular, gained attention as a result of the challenges associated with obtaining repeatable findings and raising ZT over one. For developing and calculating the prospective of a thermal system, the Fig. of merit is employed [25, 26].

$$ZT = \frac{S^2 \sigma T}{\kappa} \tag{1}$$

where S is Seebeck coefficient, σ is electrical conductivity, T is absolute temperature, κ is the total thermal conductivity, which is the sum of electronic thermal conductivity (κ_e) and lattice thermal conductivity (κ_l) as $\kappa = \kappa_e + \kappa_l$. The term $S^2\sigma$ is termed as power factor. However, for optimizing ZT, altering the charge recombination to strike the right balance between a maximum $S^2\sigma/\tau$ and a minimum κ is essential [27, 28]. The material's electronic and phonon band structures were analyzed to play a crucial role in determining its efficiency [13]. When choosing a suitable thermoelectric material, a high value of ZT is not only the factor to consider. There have been reports that lowering ZT to improve power performance is beneficial [29]. An exclusive focus on ZT obscures the significance of power production, a parameter in which the HH alloys excel. There have been numerous reports of new materials that are thermoelectrically effective, such as p-type PbTe-SrTe, which has a maximum ZT of 2.5, Bi_2Te_3 and Sb_2Te_3 bilayers, which have a ZT of 2.4, and SnSe, which has a ZT of 2.6 [30]. Ti/Sn doped NbFeSb and TaFeSb heuslers have been shown to attain ZT values of 1.1 and 0.5 [31], respectively, in experimental studies[32]. A few alloys that are worth mentioning are the following: p-type TiPdSn, n-type XNiSn, p-type Fe(V,Nb)Sb, p-type XCoSb (X = Ti, Zr, Hf), and TaIrSn. These alloys have high ZTs and may exhibit high-temperature TE efficiency [33]. These suggest that the study of novel HHs will result in a higher Fig. of merit. Some recent studies on various half-Heuslers [31, 34–63] have also shown remarkable performances. The outcomes mentioned above motivated us to find out more about HH compounds [64–68]. Using first-principles calculations, we have examined the structural, elastic, electronic, optical, and thermoelectric characteristics of RhZrX (where X = P, As, Sb, Bi) HH compounds. These materials are of great importance because of their remarkable simple cubic structure with excessive band gap, mechanical and dynamical stability, high electrical conductivity, low thermal conductivity, excellent absorption in UV–VIS region, less reflectance, prodigious optical performances. To the best of our knowledge, no previous studies have investigated these compounds that haven't been thoroughly examined. Accurate computation of the electronic band structure is necessary to replicate convincing results of related properties. Since it has been demonstrated that Tran-Blaha modified Becke-Johnson exchange (TB-mBJ) potential can predict the band gap of solids rather well, we apply it in our study. Our results suggest that the materials examined in the present study would be of great choice for use in optoelectronic and thermoelectric generators. We hope that the findings of the present study will be useful in future experimental and theoretical studies of other HH chemicals. The paper is organized as

follows: The computational methodology and variables are introduced in the second section. The results are then presented, together with an evaluation and discussion of them, in the third section. The significant successes of the present work are listed along with a conclusion in the last section.

2 Methodology

The computations were carried out for computing the structural and phonon dispersion using full potential linearized augmented plane-wave plus local orbitals method described in previous literature [69, 70]. Further, generalized gradient approximation (GGA) of Perdew, Burke, and Ernzerhof (PBE), TB-mBJ plus spin-orbital coupling (TB-mBJ + SOC) are utilized [69–71]. Typically, the band gap of semiconductors is underestimated by PBE-GGA [72] as its failure to underestimation is caused by not taking into consideration the self-energy of the quasiparticle [73]. This issue is addressed by utilizing the TB-mBJ potential, which provides a more accurate calculation regarding the band structure of electronic systems thus, improves the computation of the band gap. In the present work, the PBE-GGA, mBJ and mBJ + SOC techniques are used to calculate the electrical characteristics [74–77]. Similar to this, to check the optical nature of RhZrX (X = P, As, Sb, Bi) HH alloys we computed the optical properties by using the mBJ approximation. Using the mBJ approximation, the electron–electron correlation effect [78–80] is handled. The Rh, Zr, P, As, Sb, and Bi atoms have muffin tin radii (R_{MT}) of 1.24, 1.25, 1.24, 1.25, 1.32, and 1.61 a.u., respectively. With angular moments up to $I_{max} = 10$, the spherical harmonic expansion is used to represent the charge density and potentials. We employ a plane wave basis with an $R_{MT} \times K_{max} = 9$ cutoff. For the Brillouin zone integration, a mesh of 1000 k-points enables convergence and total energy reduction. The energy difference between the valence and core states was set at -8 Ry. Charge convergence was performed at 0.0001 Ry. The IR_ELAST method was used to compute the elastic constants and implemented in WIEN2k [81]. For the calculation of phonon vibrational properties, the Phonopy software [72] was employed, which employed the force constant method based on density-functional perturbation theory within the quasi-harmonic approximation of phonon frequencies. A $2 \times 2 \times 2$ supercell was built, and self-consistency computations were carried out under the GGA approximation using the WIEN2k code [81] to obtain the phonon density of states (DOS) and dispersion relation. The thermoelectric characteristics of the studied half Heusler alloys were examined utilizing Boltzmann's semi-classical theory and Boltztrap method [82]. τ value is assumed to be a constant, and its typical value is around 10^{-14} *s*.

3 Result and Discussion

3.1 Structural Properties

Ternary RhZrX (X = P, As, Sb, Bi) HH alloys, which are crystallized in cubic F $\bar{4}$ 3 m (No. 216) space group, have an n-type structure, shown in Fig. 1. The ternary HH has the typical form, the elements in XYZ, consists of a main group element Z along with two transition metals X and Y. Three distinct nonequivalent atomic configurations are possible for each HH. Type 1 comprises X (0, 0, 0), Y (0.5, 0.5, 0.5), and Z (0.75, 0.75, 0.75); Type 2 comprises X (0, 0, 0), Y (0.25, 0.25, 0.25), and Z (0.75, 0.75, 0.75); and Type 3 comprises X (0.5, 0.5, 0.5), Y (0, 0, 0), Z (0.75, 0.75, 0.75). By calculating their minimum energy, we conducted a straightforward investigation to determine the most favorable structure. To acquire the optimized lattice constant, we utilized Birch Murnaghan's equation of state to fit the energy vs volume data, as explained in Eq. 1 of Ref [83]. Here, V and V_0 denote the unit cell volumes at normal conditions and ground state, respectively, while B_0 represents the bulk modulus and B_0' is its pressure derivative at $V = V_0$. Figure 2 (a-d) displays the energy versus volume curves for RhZrX (X = P, As, Sb, Bi) HHs, and Table 1 contains the computed data. Our findings on structural factors are presented in Table 1. The lattice constants of RhZrX (X = P, As, Sb, Bi) compounds are computed as 5.97, 6.11, 6.29 and 6.39 Å, respectively. The calculated values of lattice constants are consistent with the values reported in materials project [84]. The computed bulk modulus (57.22 GPa, 87.67 GPa, 137.67

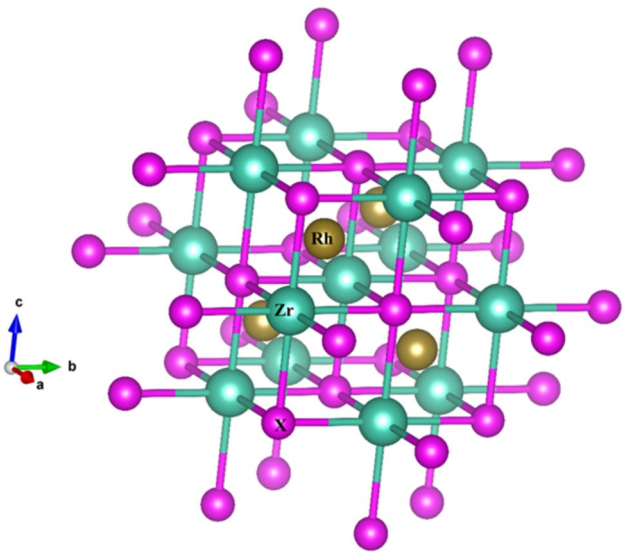

Fig. 1 The computed cubic F $\bar{4}$ 3 m structure of ternary RhZrX (X = P, As, Sb, Bi) HH alloys generated by VESTA code

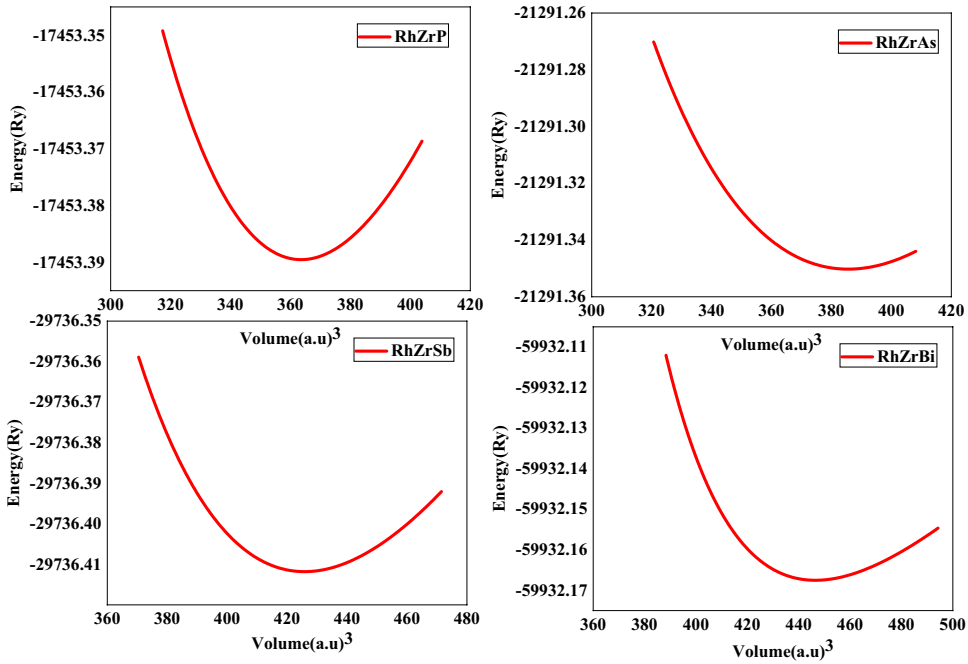

Fig. 2 Energy versus volume for optimization of RhZrX (X = P, As, Sb, Bi) alloys in cubic F $\overline{4}$ 3 m structure

Table 1 Ground state properties of RhZrX (X = P, As, Sb, Bi) HH alloys at 0 GPa nd 0 K: Structural parameters i.e., lattice parameter (a_0), unit cell volume (V_0), bulk modulus (B_0), pressure derivative of B_0, total minimum energy E_0, cohesive energy (E_{coh}), formation energy (E_{form}) and Bond length

Compound	a_0 (Å)	V_0(a.u^3)	B_0 (GPa)	B_0'	E_0(Ry)	E_{coh} (eV/atom)	E_{form}	Bond length (Å)
RhZrP	5.97	360.61	191.56	3.40	− 17,453.388886	6.01	− 1.104	Rh-Zr = 2.58 Rh-P = 2.58 Zr-P = 2.98
RhZrAs	6.11 6.28 [84]	385.54	153.62	4.52	− 21,291.350246	5.66	− 1.007	Rh-Zr = 2.64 Rh-P = 2.64 Zr-P = 3.05
RhZrSb	6.29 6.52 [84]	420.98	173.30 163.2 [43] 143.472 [44] 151.12[44]	3.57	− 29,736.409598	5.39	− 1.003	Rh-Zr = 2.72 Rh-P = 2.72 Zr-P = 3.14
RhZrBi	6.39 6.64 [84]	441.27	160.53 132.38[45]	3.77	− 59,932.163928	4.41	− 0.724	Rh-Zr = 2.76 Rh-P = 2.76 Zr-P = 3.19

GPa and 157.01 GPa) and Pugh ratio (1.43, 1.66, 1.94, and 2.77) for RhZrX (X = P, As, Sb, Bi) HH are also reported, respectively.

To confirm the structural stability of RhZrX (where X = P, As, Sb, Bi), the cohesive energy (E_{coh}) is calculated using the following equation [34, 35]:

$$E_{coh} = \frac{[E_{Rh}^{atom} + E_{Zr}^{atom} + E_{X}^{atom}] - E_{tot}^{RhZrX}}{n} \quad (2)$$

where E_{tot}^{RhZrX} is total energy of RhZrX (X = P, As, Sb, Bi) HHs in the equilibrium configuration, while the terms E_{Rh}^{atom}, E_{Zr}^{atom} and E_{X}^{atom} represent energy of isolated atom of the pure constituents, n is total number of atoms per unit cell. The calculated cohesive energies are 6.101 eV/atom, 4.774 eV/atom, and 6.512 eV/atom for RhZrP, RhZrAs, RhZrSb, and RhZrBi, respectively. Additionally, to investigate the stability, the formation energy of RhZrX (X = P, As, Sb, Bi) HHs is calculated as [34, 35]:

$$E_{form} = \frac{E_{tot}^{\mathrm{RhZrX}} - [E_{Rh}^{bulk} + E_{Zr}^{bulk} + E_{X}^{bulk}]}{n} \quad (3)$$

where the terms E_{Rh}^{bulk}, E_{Zr}^{bulk} and E_{X}^{bulk} represent energy of Rh, Zr and X = P, As, Sb, Bi in their bulk form. The computed formation energies are -1.312 eV/atom, -1.080 eV/atom,

-1.002 eV/atom, and -0.725 eV/atom for RhZrX (X = P, As, Sb, Bi), respectively. The computed formation energy suggested the stability of the studied RhZrX (X = P, As, Sb, Bi) HHs.

3.2 Phonon Calculation

The phonon dispersion was computed to determine the dynamical stability of RhZrX (X = P, As, Sb, Bi) HH alloys. Figure 3 (a-d) shows the phonon dispersion curves along with the phonon total and partial density of states in the W-L-Γ-X-W-K symmetry directions. For all RhZrX (X = P, As, Sb, Bi) alloys with the same crystal structures, it was found that the phonon dispersion band occurred near the Γ-symmetry point. After analysing the comparative phonon dispersion patterns of the investigated alloys, it was found that they adhered to the 3N relationship, where N was the total number of atoms in the primitive cell. The absence of

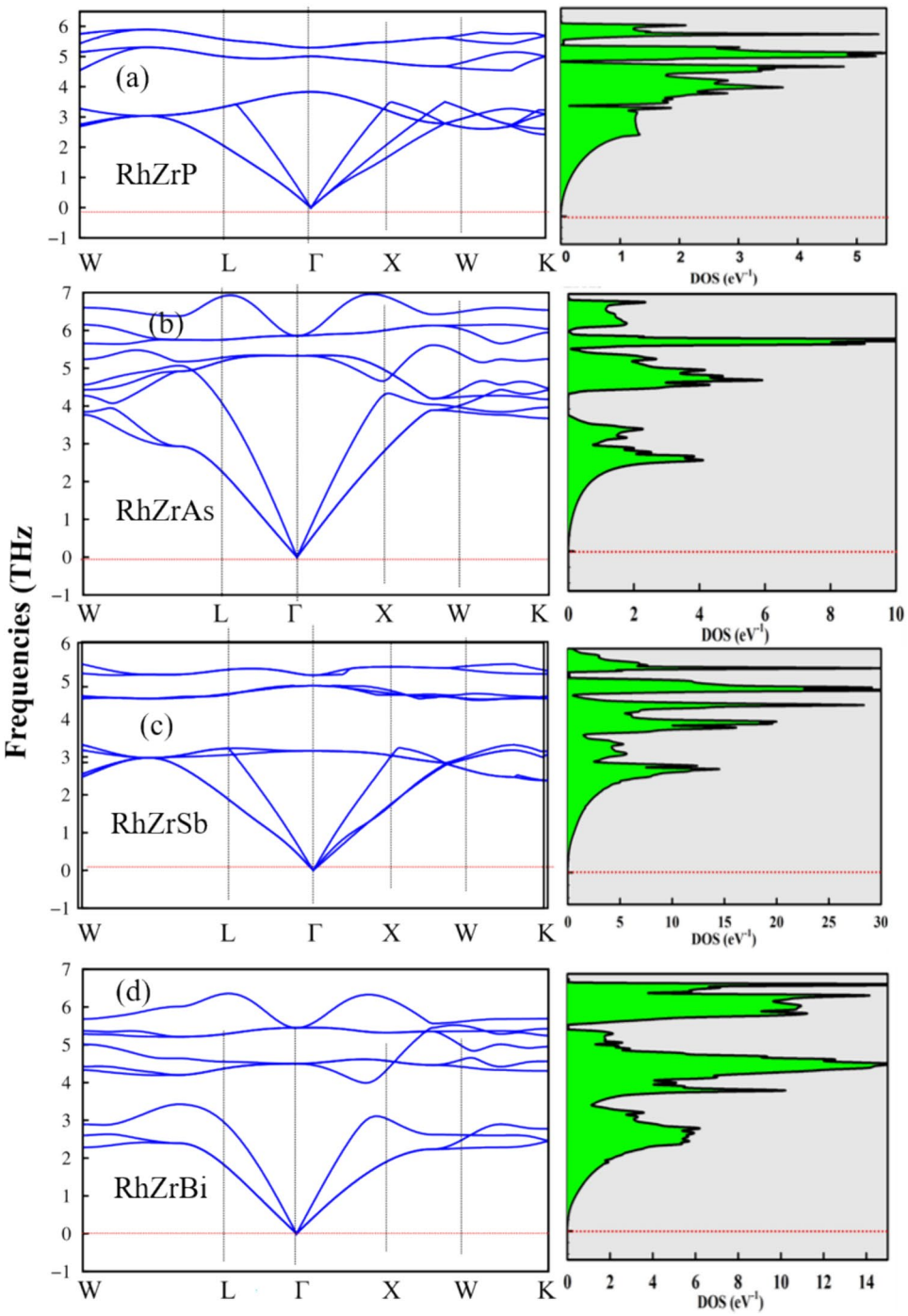

Fig. 3 The computed phonon band structure of ternary HHs RhZrX (X = P, As, Sb, Bi) alloys

unreal frequencies in any of the modes within the Brillouin zone proved the dynamical stability of the RhZrX (X = P, As, Sb, Bi) HH alloys. These findings are presented in Fig. 3. The Fig. demonstrates a total of 9 modes with 3 acoustic modes and 6 optical modes of the RhZrX (X = P, As, Sb, Bi) HH alloy. The high frequencies in the acoustic mode lead to large group velocities and significant dispersion, resulting in a considerable contribution to heat transfer from the acoustic branch, while heat transfer from the optical branches is insignificant. Phonon–phonon scattering from the interaction of acoustic and optical modes decreases a compound's lattice thermal conductivity. The thermoelectric properties section includes calculations of lattice thermal conductivity. Localized states are indicated by peaks in the phonon density of states (DOS) that correspond to the flat regions in the phonon dispersion curve. The contribution of different atoms to the phonon DOS is dependent on their mass; heavier atoms contribute to lower frequency modes, while lighter atoms contribute to higher frequency modes. From the DOS plot, it is evident that the P/As/Sb/Bi atoms of the HH compound contribute mainly to the acoustic mode of vibration. The lower optical mode has the greatest contribution from Rh atoms, whereas the upper optical mode comes from Zr atoms. The phonon dispersion spectra obtained for the considered materials are in accordance with several other HH alloys [36–39]

3.3 Mechanical Properties

The durability of a solid form as well as its resistance to external forces are significantly influenced by its mechanical characteristics, which are linked to fundamental solid-state phenomena including interatomic bonding, phonon spectrum, and equation of state. The IR-elast package integrated into WIEN2k is used to generate the independent elastic constants C_{11}, C_{12} and C_{44} (only three in cubic case), which are used to derive mechanical parameters and are listed in Table 2. According to the computations, these compounds satisfy the Born mechanical stability conditions, which include $C_{11}+2C_{12}>0$, $C_{44}>0$, $C_{11}- C_{12}>0$, and $C_{12}<C_{11}$ [85], indicating that they are a mechanically stable perovskite form. The elastic constants for cubic structures, including the bulk modulus (B), shear modulus (G), Young modulus (Y), Poisson's ratio (v), and anisotropy (A), are determined using the following formulations [40].

$$\boldsymbol{B} = \frac{\boldsymbol{C}_{11} + 2\boldsymbol{C}_{12}}{3} \tag{4}$$

$$\boldsymbol{G} = \frac{\boldsymbol{C}_{11} - \boldsymbol{C}_{12}}{2} \tag{5}$$

$$\boldsymbol{Y} = \frac{9\boldsymbol{GB}}{3\boldsymbol{B} + \boldsymbol{G}} \tag{6}$$

$$\boldsymbol{v} = \frac{3\boldsymbol{B} - 2\boldsymbol{G}}{2(3\boldsymbol{B} + \boldsymbol{G})} \tag{7}$$

$$\boldsymbol{A} = \frac{2\boldsymbol{C}_{44}}{\boldsymbol{C}_{11} - \boldsymbol{C}_{12}} \tag{8}$$

The resistance of a material to volume change can be determined by its bulk modulus (B) when it is compressed. A high value of B indicates strong crystal strength, while the crystal's resistance to plastic deformation is indicated by the shear modulus (G). The estimated values of B for RhZrX (where X can be P, As, Sb, or Bi) also provide 57.22 GPa, 87.67 GPa, 137.16 GPa, and 159.01 GPa, respectively. The results suggest RhZrSb and RhZrBi are more robust to the volume change than RhZrP and RhZrAs due to higher B values. Additionally, RhZrSb has a higher G value than other HHs suggesting it is more resistant to transverse bending. The material brittleness or ductility can be quantified by Pugh's ratio (B/G). If the B/G ratio is more than 1.75, the crystal is ductile; if not, it is brittle. Table 2 displays the estimated B/G for RhZrX (X = P, As, Sb, Bi) HHs demonstrating the brittle nature of RhZrSb and RhZrBi. Frantsevich et al. used Poisson's ratio (v) to distinguish between brittleness and ductility; 0.26 is the critical value for both brittle and ductile qualities. The compound is brittle when the falls below 0.26; ductile when the climbs over 0.26. The RhZrX (X = P, As), have estimated its values of 0.21 and 0.24, respectively, showing the brittle nature. The compounds being studied are found to be ductile, as indicated by their Cauchy pressure values, which are calculated using the formula $C^p = C_{12}—C_{44}$ and are presented in Table 2. The sign of the Cauchy pressure value, whether positive or negative, can serve as an indicator of the type of crystal bond, whether ionic or covalent. For the RhZrX (X = P, As, Sb, Bi) HHs, the negative Cauchy pressure values indicate the corresponding bonding character. Additionally, crystals with A values between 0 and 1 are considered anisotropic, while those with an A value of 1 are considered isotropic. The studied RhZrX (X = P, As, Sb, Bi) HHs, is found to be anisotropic. Two thermodynamic factors associated with elastic properties—study also involved an analysis of the 544 point T_m and the Debye temperature (θ_D). θ_D was calculated using the mean sound velocity and the formula [41] for V_m using Eq. (10).

$$\theta_D = \frac{h}{K_B}\left[\frac{3n}{4\pi}\left(\frac{N_A\rho}{M}\right)\right]^{-1/3} V_m \tag{9}$$

Here, 'n' represents the total count of atoms present in a single cell, Avogadro's number is N_A, Plank's constant is h, and k is Boltzmann's constant, ρ is density of the materials,

Table 2 Mechanical properties of RhZrX (X = P, As, Sb, Bi) HH alloys: Elastic constants (C_{ij}), bulk modulus (B), shear modulus (G), Young's modulus (E), Poisson's ratio (σ), Pugh ratio (B/G), Cauchy pressure C^P, sound velocities (m/s), Debye Temperature Θ_D (K) and melting temperature (T_m)

Material property	ZrRhP	ZrRhAs	ZrRhSb	ZrRhBi	Others
C_{11} (GPa)	91.67	134.42	217.67	243.54	221.89[42] 295.75[43] 230.71[44] 212.56[44] 262.9[45]
C_{12}(GPa)	40.00	64.29	96.91	116.74	82.07[42] 92.13[43] 86.69[44] 100.83[44] 62.72[45]
C_{44}(GPa)	49.11	64.37	77.20	69.20	33.97[42] 77.23[43] 77.38[44] 73.83[44] 45.42[45]
Bulk modulus, B (GPa)	57.22	87.67	137.16	159.01	135.44[43] 129.44[44]
Shear modulus, G (GPa)	39.80	52.65	70.47	66.88	44.307[42]
Young modulus, E (GPa)	96.23	131.60	180.50	175.97	118.94[42] 170.85[43] 190.17[44]
Poisson ratio, σ (GPa)	0.21	0.24	0.28	0.31	0.342[42] 0.27[43] 0.264[44] 0.292[44] 0.278[45]
Pugh ratio, B/G (GPa)	1.43	1.66	1.94	2.77	2.837[42]
Cauchy pressure C^P (GPa)	−9.11	−0.08	19.71	47.54	48.09[42] 11.97[43]
Transverse sound velocity, v_t (m/s)	2110	2450	2879	2554	2516.93[42] 3050[43]
Longitudinal sound, v_l velocity(m/s)	3557	4293	5225	4921	5139.69[42] 5621[43]
Average sound velocity, V_m (m/s)	2337	2722	3209	2858	2836.89[42]3403[43] 3384.51[44] 3591.53[44]
Temperature θ_D (K)	284.5	310.9	347.8	304.7	320.49[42] 353.0[43] 402[44]
Melting temperature T_m(K)	1095.8	1348.5	1840.6	1993.6	

M is molecular weight. Table 2 contains the computed Debye temperature. The investigated materials' mean sound speeds were determined using [41, 42]

$$V_m = \left[\frac{1}{3}\left(\frac{2}{v_l^3} + \frac{1}{v_t^3}\right)\right]^{-(1/3)} \tag{10}$$

Further, Table 2 displays the calculated values of υ_t, υ_l, V_m, θ_D, and T_m, which are utilized to ascertain the longitudinal and transverse components of sound velocity, using the shear modulus and bulk modulus, respectively. The results obtained on mechanical properties and presented in Table 2 for the considered materials, are in accordance with the other similar HH alloys [43–45].

$$v_t = \sqrt{\frac{G}{\rho}} \tag{11}$$

$$v_l = \sqrt{\frac{3B + 4G}{3\rho}} \tag{12}$$

3.4 Electronic Properties

Figure 4 illustrates a non-spin polarized band structure analysis of RhZrX along the high symmetry directions W-L-Γ-X-W-K in the first Brillouin zone's irreducible part. All compounds were observed to have a small indirect band gap with the Fermi level set at zero energy. The mBJ approximation's red lines and the GGA approximation's green lines are represented in the Figs. The VBM and CBM of RhZrP, RhZrAs, RhZrSb, and RhZrBi were observed to be at the Γ and X point, respectively. Table 3 presents the computed band gap values from mBJ approximations, with RhZrAs having the highest band gap value of 1.426 eV and RhZrBi having the lowest at 1.077 eV. To analyze the material

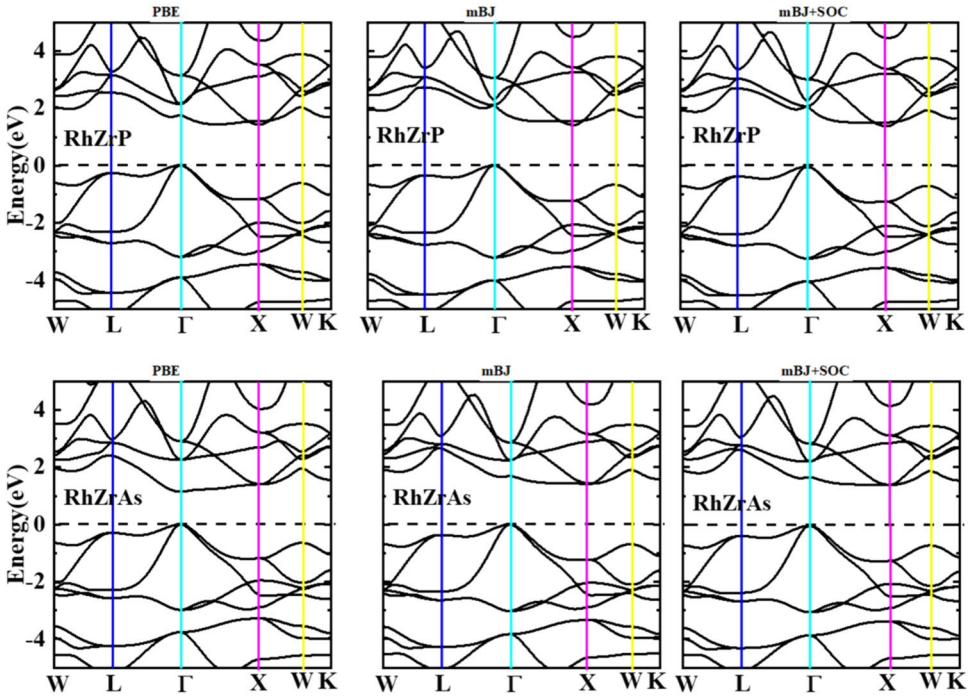

Fig. 4 The computed electronic band structure of HH RhZrX (X = P, As) alloys which are employed with diverse approaches

Table 3 Calculated energy band gap of RhZrX(X = P, As, Sb, Bi).using PBE-GGA, TB-mBJ, and TB-mBJ + SOC potentials

Properties	PBE-GGA	TB-mBJ	TB-mBJ + SOC	Others
RhZrP	1.35	1.414	1.32	0.955 [43] 1.0 [44] 1.007 [44]
RhZrAs	1.38	1.426	1.34	
RhZrSb	1.140	1.209	1.14	
RhZrBi	1.04	1.077	0.970	

nature and to get the best semiconductor, we calculated the electronic band structure of all RhZrX (X = P, As, Sb, Bi) HH alloys with diverse approximations such as PBE-GGA, mBJ, and mBJ + SOC. We computed the electronic band gap with energy (eV) along the y-axis and K-wave vector along the x-axis for all RhZrX (X = P, As, Sb, Bi) HH alloys. For RhZrP alloy with GGA, mBJ, and mBJ + SOC, we determined the indirect [Γ-X] band gap values 1.40 eV, 1.42 eV, and 1.34 eV as shown in Fig. 4. Similarly, for RhZrAs alloy with GGA, the direct [Γ-Γ] band gap value is 1.10 eV but with mBJ, and mBJ + SOC, we determined indirect band gap [Γ-X] values are 1.42 eV, and 1.37 eV as exhibits in Fig. 5. Additionally, we also mentioned all computed values of HH alloys in Table 3 with diverse approximations. These results are compared with the similar HH alloys [31, 43–46] and results are in good agreement. The band profile is in match with the other HH materials [46, 47]

The combined TDOS and PDOS of RhZrX (X = P, As, Sb, Bi) are shown in Fig. 6(a, b), providing detailed information on the contribution of each element. The density of state contours indicates that Rh atom, with minor contributions from Zr/X atoms create a top of the valence band (VC) in the energy range of -4 eV to 0 eV in the examined RhZrX (X = P, As, Sb, Bi) compounds. Meanwhile, the bands in the energy range of 0 eV to 4 eV are primarily due to the Zr and a minor contribution from Rh atoms, with P/As/Sb/Bi atoms. Finally, the bands forming within the higher energy level of the conduction band (CB) result from the hybridization of the group of Zr atoms and a small P/As/Sb/Bi atom. Tables 4 and 5 present computations of the transition of carriers from maximum occupied states to unoccupied states for HH alloys with Bader charge and effective mass, for studied RhZrX (X = P, As, Sb, Bi) HHs.

3.5 Optical Properties

For the study of the optical and electronic transport properties of the RhZrX (P, As, Sb, Bi), HHs the possibility of utilizing their fascinating electronic structure for the applications in optoelectronic semiconductors was the driving force behind the motivation. Dielectric functions are used to explore and determine energy dependent optical properties. It is known that the complex dielectric function ε(ω), has

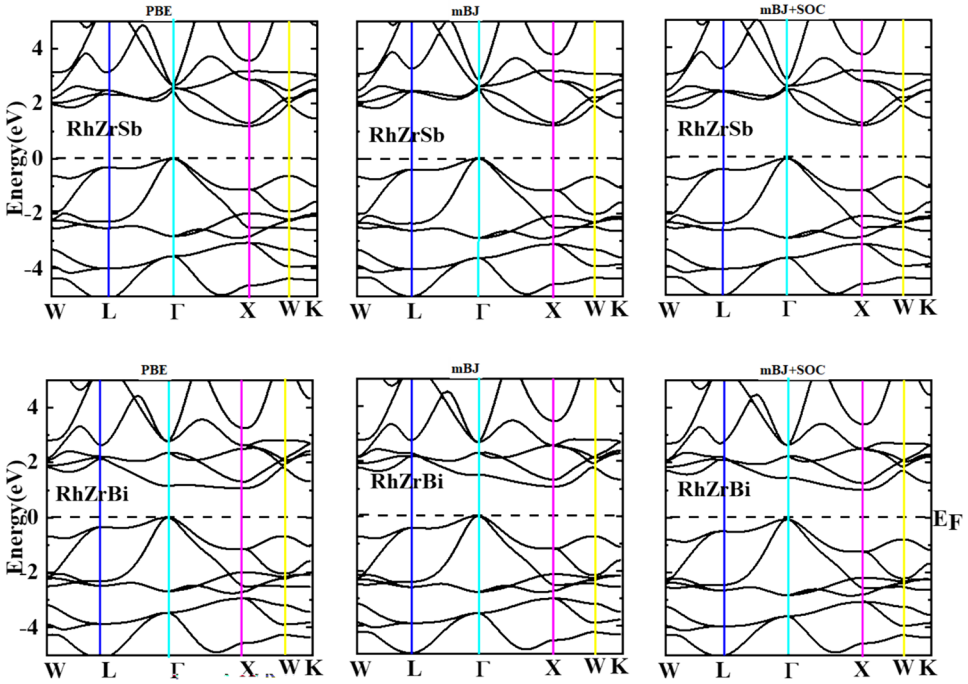

Fig. 5 The computed electronic band structure of RhZrX (X = Sb, Bi) HH alloys which are employed with diverse approaches

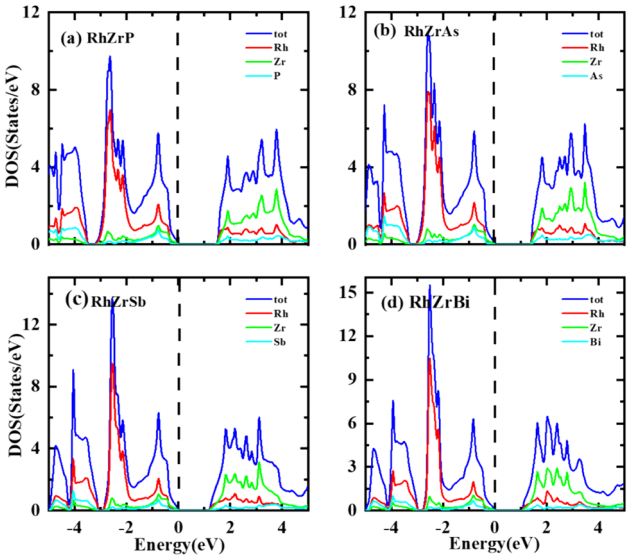

Fig. 6 The computed electronic properties with a total and partial density of states of **a** RhZrP **b** RhZrAs **c** RhZrSb **d** RhZrBi HH alloys which are employed with mBJ approaches

two parts namely imaginary and real, represents the optical characteristics of a solid which can be expressed as [86–88]

$$\varepsilon = \varepsilon_1(\omega) + i\varepsilon_2(\omega) \tag{13}$$

Mathematically defined, the imaginary part $\varepsilon_2(\omega)$ results from both inter-band and intra-band transitions and indicates potential transitions from occupied to unoccupied states at fixed (k-vectors) over the Brillouin zone (BZ). These transitions are influenced by the density of states (DOS) and momentum matrix P.

$$\varepsilon_2(\omega) = \frac{e^2\hbar}{\pi m^2\omega^2} \sum \int \left|M_{v,c}(k)\right|^2 \delta[\omega_{vc}(k) - \omega] d^3k \tag{14}$$

The crystal wave functions are represented by c_k and v_k, while p denotes the element of the moment matrices between the band states of and within the crystal momentum k, which is determined using the Kramers–Kronig connection. This yields the real component $\varepsilon_1(\omega)$ of the dielectric function for the conduction and valence bands with the crystal wave vector k, with the imaginary part determining the same [87, 88].

Table 4 Calculated Bader charges of RhZrX(X = P, As, Sb, Bi) using PBE-GGA, TB-mBJ, and TB-mBJ + SOC potential

Bader Charges								Others [42]	
Zr	1.63	Zr	1.58	Zr	1.50	Zr	1.44	Nb	0.829
P	−0.86	As	−0.71	Sb	−0.47	Bi	−0.22	Ag	−0.378
Rh	−0.77	Rh	−0.86	Rh	−1.14	Rh	−1.21	Si	−0.452

Table 5 Calculated effective mass of RhZrX(X = P, As, Sb, Bi) using PBE-GGA, TB-mBJ, and TB-mBJ + SOC potential

Effective mass			
ZrRhP	ZrRhAs	ZrRhSb	ZrRh As
Hole 1.77	Hole 1.85	Hole 2.58	Hole 2.66
Electron 0.18	Electron 0.14	Electron 0.05	Electron 0.03

$$\varepsilon_1(\omega) = 1 + \frac{2}{\pi} P \int_0^{\infty} \frac{\omega\prime \varepsilon_2(\omega\prime) d\omega\prime}{(\omega\prime^2 - \omega^2)} \tag{15}$$

where P is referred to as the principal value of the integral. Knowing real and imaginary parts of the dielectric function enables the calculation of the important optical properties, refractive index $n(\omega)$, extinction coefficient $k(\omega)$, reflectivity $R(\omega)$, optical absorption coefficient $\alpha(\omega)$ and optical conductivity $\sigma(\omega)$. $n(\omega)$ is [87, 88] given by Eq. (16).

$$n(\omega) = \left[\frac{\sqrt{\varepsilon_1^2(\omega) + \varepsilon_2^2(\omega)} + \varepsilon_1(\omega)}{2} \right]^{1/2} \tag{16}$$

The extinction coefficient $k(\omega)$ is determined using the computed values in $\varepsilon_1(\omega)$ and $\varepsilon_2(\omega)$ for aforesaid HHs using the following relationship [87, 88].

$$k(\omega) = \left[\frac{\sqrt{\varepsilon_1^2(\omega) + \varepsilon_2^2(\omega)}}{2} - \frac{\varepsilon_1(\omega)}{2} \right]^{1/2} \tag{17}$$

The real and imaginary components of dielectric functions are depicted in Fig. 7 (a,b) for RhZrX (P, As, Sb, Bi) HHs based on photon energy (0 eV to 12 eV). Table 6 shows that the dielectric permittivity of RhZrX (P, As, Sb, Bi) begins at 15.53, 16.19, 16.08 and 17.91 respectively, which is known as static dielectric constant $\varepsilon_1(0)$. The computed values of $\varepsilon_1(0)$ are following Penn's model as demonstrated in Fig. 7 (a) and also all static values of HH alloys are given in Table 6. Furthermore, multiple peaks are observed with photon energy which is due to the improved transition of electrons from the valence to the conduction band. Figure 7 (b) shows the variation of the imaginary dielectric constant with photon energy which quantifies absorption. Figure 7(b) shows that there is no absorption up until the visible range, after which there is a rise in absorption peak at a higher energy value. Between VB and CB, several inter-band transitions are the root cause of these observations. Fundamental absorption edge values are those that are closest to the bandgap. The optical transitions between valance band maximum (VBM) and conduction band minimum (CBM) are coincident with the primary absorption edges. On the

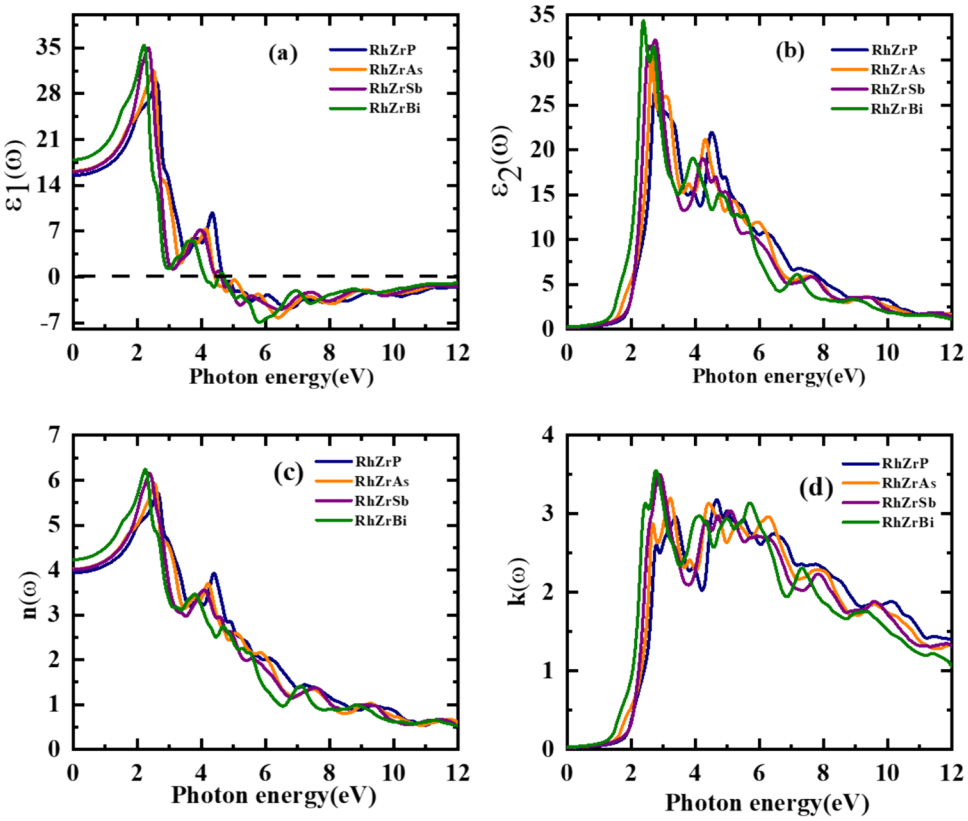

Fig. 7 The optical characteristics of RhZrX (P, As, Sb, Bi) HH alloys were determined by analyzing their **a** real dielectric function ε_1, **b** imaginary dielectric function ε_2, **c** refractive index n, and **d** extinction coefficient k as a function of photon energy (eV)

Table 6 Calculated optical parameters of RhZrX(X = P, As, Sb, Bi): Static dielectric constant $\varepsilon_1(0)$, reflectance R(0) and refractive index n(0)

	Optical parameters	RhZrP	RhZrAs	RhZrSb	RhZrBi	Others
Optical properties	$\varepsilon_1(0)$	15.53	16.19	16.08	17.91	11.38 [43], 16.1 [46] 75.89 [48], 19.49 [49] 20.30 [49], 21.02 [49]
	R(0)	0.35	0.362	0.361	0.38	0.29 [43], 0.4 [46] 0.63 [48]
	n(0)	3.94	4.02	4.01	4.23	3.37 [43], 4.0 [46] 8.79 [48], 4.43 [49] 4.50 [49],5.80 [49]

other side, there is a noticeable increase in the absorption in the UV region.

The optoelectronic properties of the studied RhZrX (P, As, Sb, Bi) HHs, which are essential for practical applications, can be understood by knowing their n (ω) and K (ω). Figure 7 (c) displays the changes of n (ω) with photon energy (eV) for RhZrX (P, As, Sb, Bi) HHs. Table 6 lists the n (ω) of RhZrX (P, As, Sb, Bi) at 0 eV energy, although the highest values of n (ω) for RhZrX (P, As, Sb, Bi) are about 3.94, 4.02, 4.01, and 4.23, respectively. In Fig. 7 (d), we calculated the energy k (ω), which denotes the dampening oscillation amplitude of the entering electric field. While there is no oscillation initially, visible zone oscillations become apparent as energy (eV) is increased. In Table 6 the calculated optical parameters are compared with the similar HH alloy [34, 46, 48, 49]. Figure 8 (a) shows a plot of electrical conductivity (σ) as a function of photon energy. The photon energy is measured in electron volt unit (eV) within the range of 0 to 12 eV. As shown in Fig. 8 (b) the σ (ω) for RhZrX (P, As, Sb, Bi) HHs begins from the threshold value and attains the maximum value 13,500 $(cm)^{-1}$, 11,200 $(cm)^{-1}$ 10,300 $(cm)^{-1}$ and 9500 $(cm)^{-1}$ respectively. Our results show that materials could be applied to various optoelectronic devices. Absorption coefficient α (ω), which indicates the amount of light the object absorbs, is another crucial optical property to study. The energy-dependent absorption spectra of RhZrX (P, As, Sb, Bi) HHs are illustrated in Fig. 8 (b). Observed substantial intensity of α (ω), for energies above 3 eV suggests that the investigated compounds are capable of absorption of visible and UV light. In Fig. 8 (c), the reflectance R (ω) of the examined RhZrX (P, As, Sb, Bi) HHs is shown over the energy spectrum from

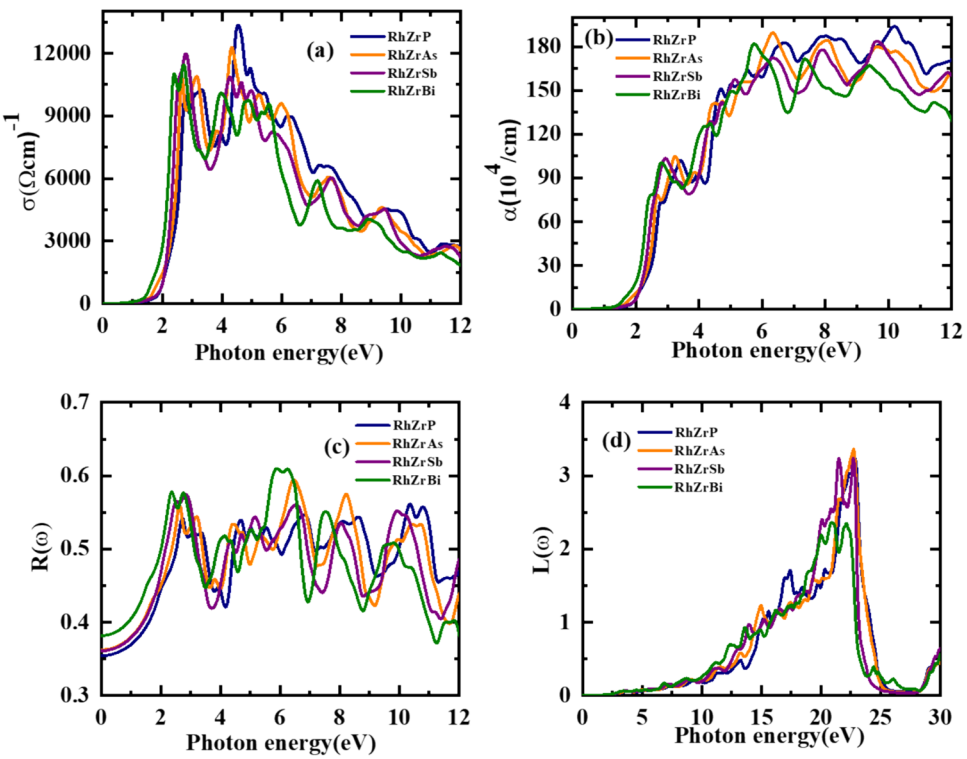

Fig. 8 The calculated optical properties of RhZrX (P, As, Sb, Bi) HH alloys with **a** electrical conductivity σ, **b** absorption coefficient α, **c** reflection R, and **d** energy loss L against photon energy (eV)

0 to 12 eV. The reflectance of RhZrX (P, As, Sb, Bi) HHs is ~ 0.35 eV at 0 eV, which indicates conventional semiconductor properties. The reflectance coefficient is observed to rise with photon energy. Another crucial optical constant for figuring out a substance's optical properties is loss function L (ω). It provides details on the compound's plasma frequencies as well as the scattering of electrons passing through them, as depicted in Fig. 8 (d). The studied compounds exhibit dielectric and semiconducting properties at energies above and below plasma frequency, respectively. RhZrX (P, As, Sb, Bi) has a maximum peak of L (ω) at a higher energy range. However, the peaks in electron energy loss coincide with the transition sites of RhZrX (P, As, Sb, Bi) HHs from semiconducting to dielectric characteristics. There are numbers of HH alloys investigated for these optical properties [50–53]. A detailed analysis of optical properties reveals their application in optoelectronics.

3.6 Thermoelectric properties

The transport characteristics of RhZrX (P, As, Sb, Bi) HH alloys are studied at three different temperatures (300 K, 600 K, and 800 K) by examining their behavior as a function of chemical potential. These HH alloys exhibit lattice stability, a high Fig. of merit, and favorable mechanical and thermal properties. Thermoelectric (TE) parameters such as Seebeck coefficient, electrical conductivity, Fig. of merit, and power factor are depicted in Fig. 9. The Seebeck coefficient (S), which measures the thermoelectric sensitivity of the material, is positive for p-type materials and negative for n-type materials. For the purpose of comprehending and characterizing the transport characteristics of charge carriers (electrons or holes) and heat in TE materials, relaxation time (τ) must be included in the parameters [68, 89, 90]. Based on the Seebeck, Peltier, and Thomson effects, TE materials transform thermal energy into electrical energy or the other way around. The τ represents the mean amount of time that passes between consecutive charge carrier collisions with the material's scattering centres, phonons, or lattice defects. It has a significant impact on electrical and thermal conductivity by defining the transport characteristics of charge carriers and phonons. Therefore, to effectively forecast and optimize a material's TE performance, τ must be taken into account while calculating TE parameters. Longer relaxation durations are typically associated with improved charge carrier mobility and less scattering, which improve electrical conductivity and, in turn, TE efficiency.

Figure 9 (a) illustrates the dependence of S on temperature, which shows an increase in S with increasing temperature for optimal thermoelectric performance. At 300 K, the S for RhZrX (P, As, Sb, Bi) HHs is determined to be 239 μV/K, 231 μV/K, 235 μV/K, and 236 μV/K, respectively. The positive value of S reflects the majority of charge carriers are p-type. Furthermore, to have good

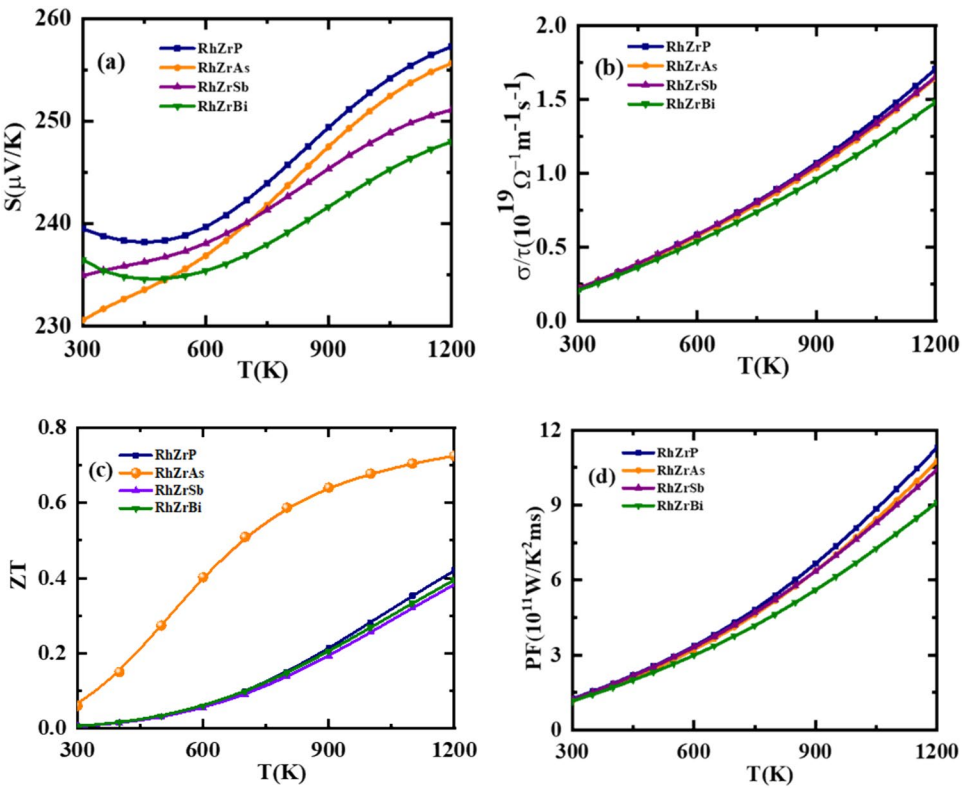

Fig. 9 The calculated transport properties of RhZrX (X = P, As, Sb, Bi) HH alloys with the **a** Seebeck coefficient S, **b** electrical conductivity σ/τ, **c** Fig. of merits ZT, and **d** power factor PF against temperature T (K)

thermoelectric performance the S ≥ 200 μV/K suggests significant thermoelectric properties of the studied RhZrX (P, As, Sb, Bi) HHs. The estimated electronic conductivity (σ/τ) for RhZrX (P, As, Sb, Bi) HHs is represented in Fig. 9 (b). At room temperature it is found to be 2.17×10^{18} $(\Omega mS)^{-1}$, 2.23×10^{18} $(\Omega mS)^{-1}$, 2.28×10^{18} $(\Omega mS)^{-1}$, and 2.07×10^{18} $(\Omega mS)^{-1}$, respectively. The σ/τ is observed to increase with an increase in temperature which suggests typical semiconductor characteristics. Figure 9 (c) demonstrates the dimensionless Fig. of merit (ZT) against temperature (K) with a 300 K difference. The ZT is considered for RhZrX (X = P, As, Sb, Bi) HHs alloys at room temperature (300 K), which has a minimum value for all HH alloys, except RhZrAs. The nature of ZT for RhZrAs is quite different because it sharply increases as compared to other HHs alloys. We attend the maximum value of ZT at 1200 K for each HH alloy is RhZrX (X = P, Sb, Bi) 0.4, 0.7, 0.38 and 0.37, respectively. We concluded that the RhZrAs alloy is a good candidate for thermal devices due to having the highest values as compared to the other alloys. The efficiency of the thermoelectric materials can be quantified from the power factor ($S^2\sigma$) which is represented in Fig. 9 (d). With temperature, the power factor is observed to increase and at 1200 K it is found to be 1.25×10^{11} W/K^{2}ms, 1.19×10^{11} W/K^{2}ms, 1.22×10^{11} W/K^{2}ms, and 1.16×10^{11} W/K^{2}ms, the high power factor at higher temperature suggest the optimum thermoelectric response of the investigated RhZrX (P, As, Sb, Bi) HHs. Our calculated results on Seebeck coefficient and electrical conductivity as depicted in Fig. 9 are consistent with the other HH alloys [54].

In addition, we included the room temperature values of transport properties for RhZrX (P, As, Sb, Bi) in Table 7, our results are in agreement with the other HH alloys [55]. The effective mass, denoted as m*, was determined (Table 5) using the parabolic band approximation method [56, 57], by fitting the wave vector (K) vs energy (E) of the CBM or the VBM, depending on the type of charge carriers present.

$$m^* = \frac{h^2}{dE^2/dK^2} \tag{18}$$

The ZT, which is also referred to as the maximum efficiency condition, is a crucial parameter used in the calculation of efficiency and can be calculated by Eq. (1).

Slack's equation [80] is used to derive the phononic component of thermal conductivity (κ_l).

$$k_l = A\frac{M\theta_D^3\delta}{\gamma^2 n^{2/3}T} \tag{19}$$

The thermoelectric Fig. of merit is determined by integrating the outcomes of resolving Slack's and Boltzmann transport equations, taking into account the average molecular weight (M), the number of atoms per unit cell (n), the absolute temperature (T), the Grüneisen parameter (γ), the Debye's temperature (θ_D), and a coefficient (A) that relies on γ and is expressed in units of W mol/kg/m^2/K^2.

Figure 10 (a-d) determined the thermal conductivity which is the sum of the phonon thermal conductivity (κ_l) and electronic thermal conductivity (κ_e) for each alloy. Figure 10 (a) shows the thermal conductivity of RhZrP alloy against temperature (K), here red line presents the electronic thermal conductivity, the blue line represents the total thermal conductivity and the black line demonstrates the lattice thermal conductivity. As we have analyzed that initially at room temperature (300 K), lattice thermal conductivity is higher as compared to the electronic thermal conductivity. However, by increasing the temperature, κ_l gradually decreases but κ_e increases at a higher temperature. Similarly, we found the same nature in all computed alloys' thermal conductivity which is shown in Fig. 10 (c-d). However, we observed the quite different nature of the total thermal conductivity of each RhZrX (P, As, Sb, Bi) HH alloys having the different values 6.55×10^{15}W/mKs, 0.584×10^{15}W/mKs, 7.089×10^{15}W/mKs, and 5.59×10^{15}W/mKs respectively. Similar optical, transport, electronic studies under the

Table 7 Calculated transport parameters of RhZrX(X = P, As, Sb, Bi) HH alloys at 300 K: Electrical conductivity (σ/τ), carrier concentration (n), Seebeck coefficient (S), Hall coefficient (R_H), electronic thermal conductivity (k_e), lattice thermal conductivity (k_l), total thermal conductivity (κ_{tot}), Fig. of merit (ZT), power factor (PF)

	Transport parameters	RhZrP	RhZrAs	RhZrSb	RhZrBi	Others
Transport properties	σ/τ($10^{18}\Omega^{-1}$ m^{-1} s^{-1})	2.17	2.23	2.28	2.07	3.56 [55]
	n(e/uc)	0.0021	0.0021	0.0028	0.0025	
	S(μV/K)	239	231	235	236	226 [55]
	R_H(10^{-7}m^3/C)	1.16	1.16	1.08	1.29	
	k_e(10^{15}W/mKs)	0.049	0.048	0.049	0.045	
	k_l(10^{15}W/mKs)	6.50	0.536	7.03	5.55	
	k_{tot}(10^{15}W/mKs)	6.55	0.584	7.089	5.59	6.87 [55]
	ZT (at300K)	0.005	0.06	0.0051	0.0062	0.73 [55]
	ZT (at 1200 K)	0.42	0.72	0.38	0.39	0.75 [55]
	PF (10^{11}W/K^{2}ms)	1.25	1.19	1.22	1.16	1.79 [55]

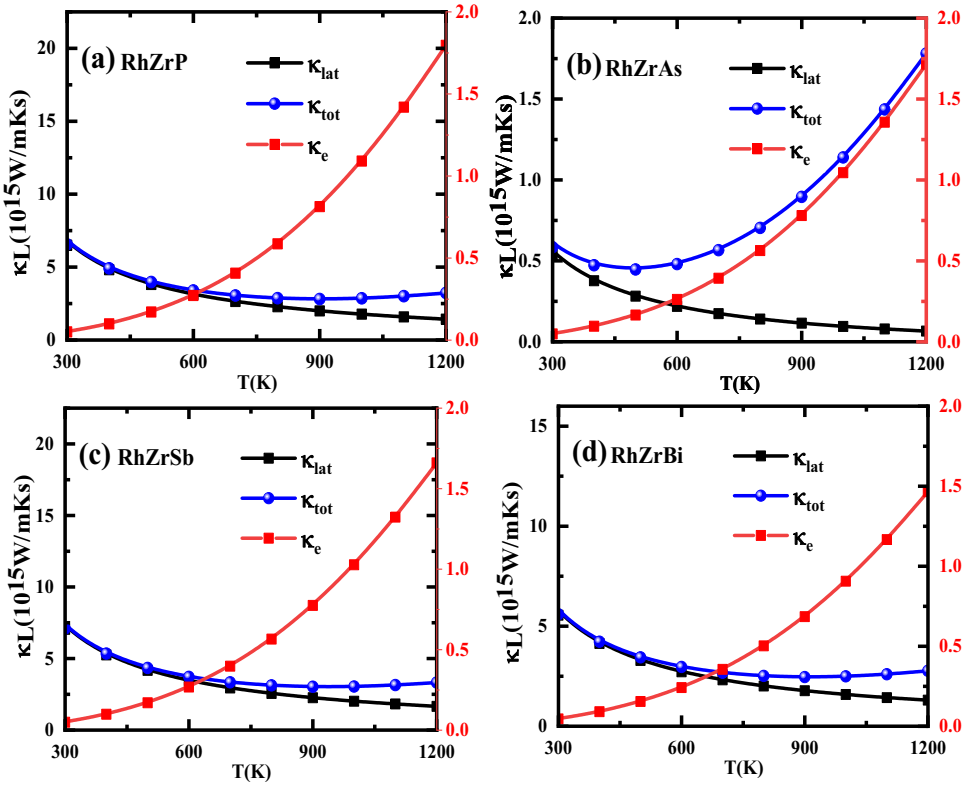

Fig. 10 Variation of thermal conductivity, κ with temperature, T: Lattice thermal conductivity (κ_l), electronic (κ_e) and total (κ_{tot}) thermal conductivity of **a** RhZrP **b** RhZrAs **c** RhZrSb **d** RhZrBi HH alloys

effect of temperature and pressure are reported [64–67, 91, 92]. There are extensive studies reported for thermoelectric performances of the HH alloys [58–63] and our results are consistent with them.

Transport properties as a function of chemical potential (μ-E_f) in eV calculated within -2 to 2 μ-E_f (eV) by using the BoltzTrap code having the interface with WIEN2k code. The positive value of chemical potential indicates that the doping is n-type and negative value represents the p-type doping. Inducing the magnitude of voltage by changing the temperature is known as Seebeck coefficient S (μV/K). S (μV/K) computed for all RhZrX (X = P, As, Sb, Bi) HH alloys with temperature variation (300 K, 600 K, 900 K, and 1200 K) as demonstrated in Fig. 11 (a-d). Figure 11 (a) represents the S (μV/K) for RhZrP alloy having red (300 K) green (600 K), light blue (900 K), and dark blue (1200 K) colors. For room temperature (red color), the Seebeck coefficient is about up to 2000 μV/K and under -2000 μV/K at 0.52 μ-E_f (eV) and 0.65 μ-E_f (eV) respectively. Similarly, for the green color, the magnitude of Seebeck coefficient is 1000 (μV/K), -1000 (μV/K) approximately at 0.5 μ-E_f (eV) and 0.68 μ-E_f (eV) correspondingly. For light blue (900 K) and dark blue (1200 K), we attained minimum Seebeck coefficient at the almost same chemical potential. Figure 11 (b) represents the S (μV/K) for As-based RhZrAs alloy having red (300 K) green (600 K), light blue (900 K), and dark blue (1200 K) color. For room temperature (red color), the Seebeck coefficient is about up to 2000 μV/K and under -2000 μV/K at 0.55 μ-E_f (eV) and 0.68 μ-E_f (eV) respectively. Similarly, for the green color, the magnitude of Seebeck coefficient is 1000 (μV/K), -1000 (μV/K) approximately at 0.52 μ-E_f (eV) and 0.69 μ-E_f (eV) correspondingly. For light blue (900 K) and dark blue (1200 K), we attained minimum Seebeck coefficient at the almost same chemical potential. Figure 11 (c) represents the S (μV/K) for RhZrSb alloy having red (300 K) green (600 K), light blue (900 K), and dark blue (1200 K) colors. For room temperature (red color), the Seebeck coefficient is about up to 2000 μV/K and under -2000 μV/K at 0.50 μ-E_f (eV) and 0.63 μ-E_f (eV) respectively. Similarly, for the green color, the magnitude of Seebeck coefficient is 1000 (μV/K), -1000 (μV/K) approximately at 0.49 μ-E_f (eV) and 0.65 μ-E_f (eV) correspondingly. For light blue (900 K) and dark blue (1200 K), we attained minimum Seebeck coefficient at almost the same chemical potential. Figure 11 (d) represents the S (μV/K) for RhZrBi alloy having red (300 K) green (600 K), light blue (900 K), and dark blue (1200 K) colors. For room temperature (red color), the Seebeck coefficient is about up to 2000 μV/K and under -2000 μV/K at 0.49 μ-E_f (eV) and 0.61 μ-E_f (eV), respectively. Similarly, for the green color, the magnitude of Seebeck coefficient is 1000 (μV/K), -1000 (μV/K) approximately at 0.48 μ-E_f (eV) and 0.64 μ-E_f (eV), correspondingly. For light blue

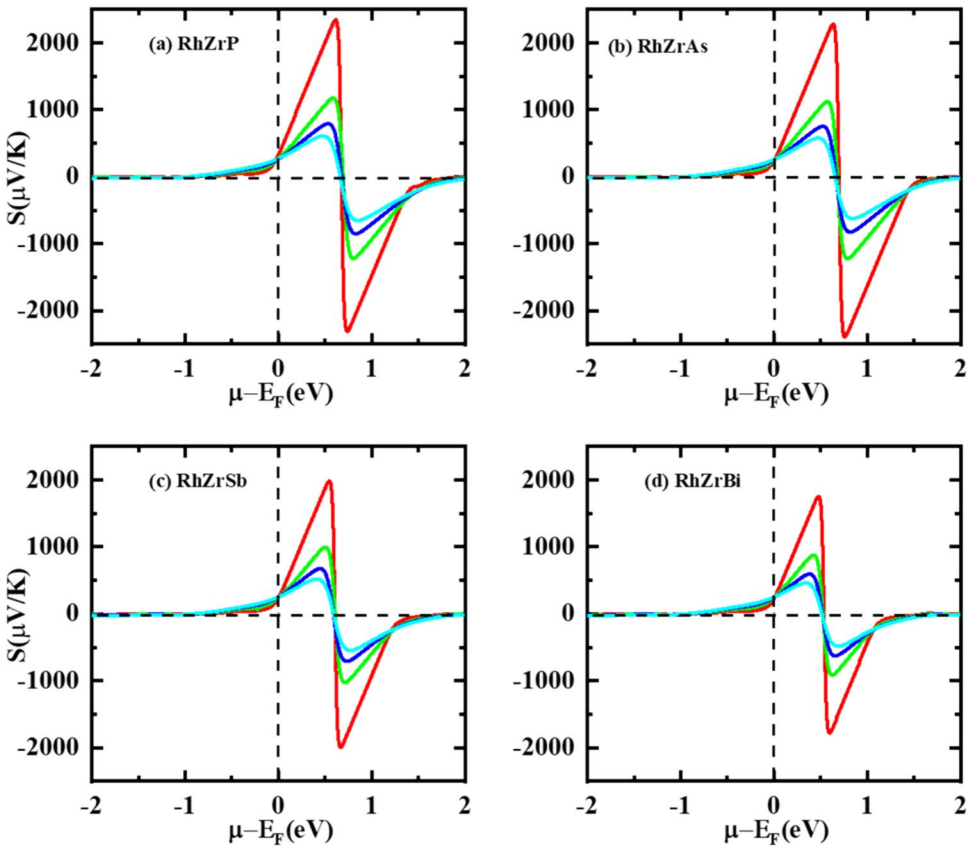

Fig. 11 The calculated Seebeck coefficient (S) of **a** RhZrP **b** RhZrAs **c** RhZrSb **d** RhZrBi HH alloys against chemical potential (μ-E_f)

(900 K) and dark blue (1200 K), we attained minimum Seebeck coefficient at almost the same chemical potential. We have analyzed that by increasing the temperature of all RhZrX (X = P, As, Sb, Bi) HHs, Seebeck coefficient decreases due to increasing phonon vibration at high temperatures. However, the maximum magnitude of Seebeck coefficient against the Sb chemical potential is at 300 K as compared to the other temperature gained for RhZrSb alloy.

As stated above the thermal conductivity is the sum of the electric and phonon vibration viz $\kappa = \kappa_l + \kappa_e$, we have computed the κ_e against the chemical potential with temperature variation (300–1200 K). κ_e for RhZrP alloy got the highest value at $11.5 \times (10^{15}$W/mKs) and $7.6 \times (10^{15}$W/mKs) with 1200 K at -1.2 μ-E_f (eV) and 2 μ-E_f (eV) respectively as demonstrated in Fig. 12 (a). By decreasing the temperature, the thermal conductivity also decreases with the minimum chemical potential in the hole doping region (negative side of x-axis) but in the electron doping region (positive side of x-axis), the potential remains the same. At room temperature, there is a minimum electronic thermal conductivity on the n-type side. Similarly, we computed the electronic thermal conductivity for RhZrAs alloy got a value under $11.5 \times (10^{15}$W/mKs) and almost $7.5 \times (10^{15}$W/mKs) with 1200 K at -1.2 μ-E_f (eV) and 2 μ-E_f (eV) respectively. Thermal conductivity has the same behavior as the previous case. At room temperature, there is a minimum electronic thermal conductivity on the n-type side as compared to the other applied temperatures as shown in Fig. 12 (b).

Like RhZrAs alloy, we have computed the electronic thermal conductivity for RhZrSb alloy and calculated a value under 9.4×10^{15}W/mKs and almost 7.1×10^{15}W/mKs with 1200 K at -1.2 μ-E_f (eV) and 2 μ-E_f (eV) respectively. Thermal conductivity has the same behavior as the previous case also. At room temperature, there is a minimum electronic thermal conductivity in the n-type side as compared to the other applied temperatures as shown in Fig. 12 (c). Lastly, we computed the electronic thermal conductivity for RhZrBi alloy got value under 9×10^{15}W/mKs and almost 7×10^{15}W/mKs with 1200 K at -1.2 μ-E_f (eV) and 2 μ-E_f (eV) respectively. At room temperature, there is minimum electronic thermal conductivity in the n-type side as compared to the other applied temperatures as shown in Fig. 12 (d).

The estimated results, comprising the carrier concentration for ranges from -2 eV to 2 eV, are displayed in Fig. 13(a). The initial peaks of RhZrP are located in the p-type area at approximately-0.99 eV with an electrical conductivity of 4.5×10^{20} (Ω^{-1} m^{-1} s^{-1}) and in the n-type region at exactly 2 eV with an electrical conductivity of 3.6×10^{20} (Ω^{-1} m^{-1} s^{-1}). By changing the temperature, we could significantly analyze the difference in electrical conductivity. Similarly, the initial peaks of for RhZrAs are located in the

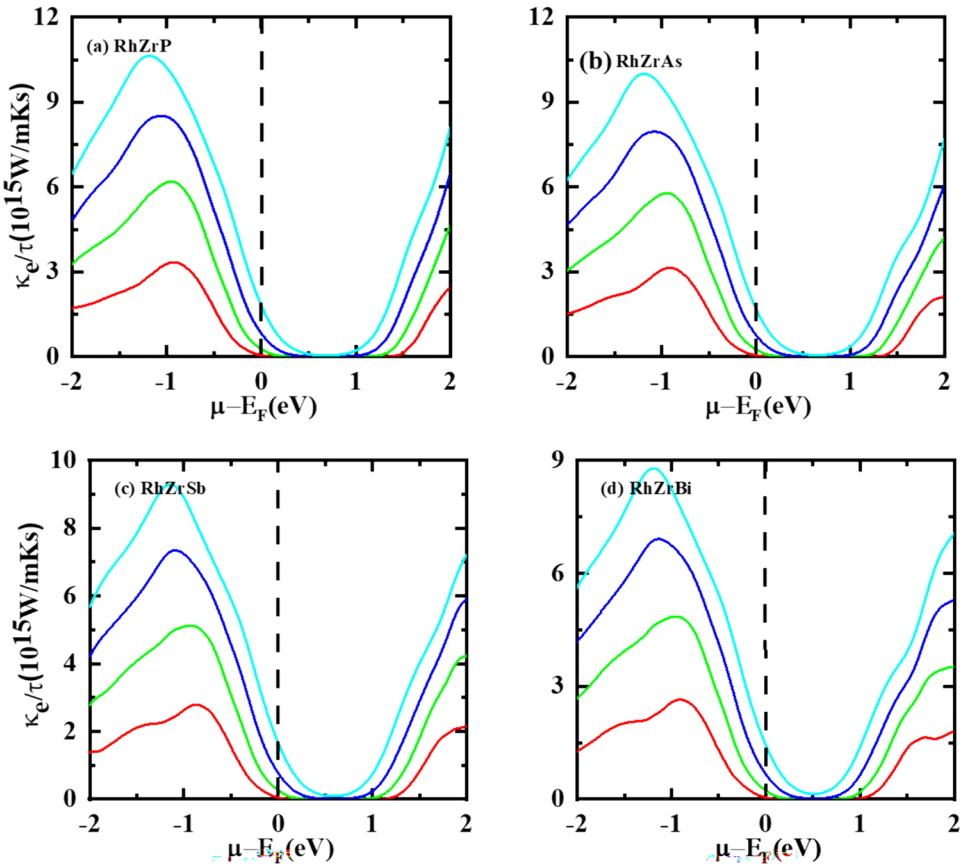

Fig. 12 The calculated electronic thermal conductivity per relaxation time (κ_e/τ) of HHs **a** RhZrP **b** RhZrAs **c** RhZrSb **d** RhZrBi HH alloys against chemical potential (μ-E_f)

p-type area at approximately -0.98 eV with an electrical conductivity of 4.4×10^{20} (Ω^{-1} m^{-1} s^{-1}) and in the n-type region at exactly 2 eV with an electrical conductivity of 3×10^{20} (Ω^{-1} m^{-1} s^{-1}) as shown in Fig. 13 (b). By changing the temperature, we could significantly analyze the difference in electrical conductivity.

Second last, the initial peaks of for RhZrSb are located in the p-type area at approximately -0.97 eV with an electrical conductivity of 4×10^{20} (Ω^{-1} m^{-1} s^{-1}) and in the n-type region at exactly 2 eV with an electrical conductivity of under 3×10^{20} (Ω^{-1} m^{-1} s^{-1}) as shown in Fig. 13 (c). Lastly, for RhZrBi alloy the initial peaks of for RhZrBi are located in the p-type area at approximately-0.96 eV with an electrical conductivity of 3.9×10^{20} (Ω^{-1} m^{-1} s^{-1}) and in the n-type region at exactly 2 eV with an electrical conductivity of 2.8×10^{20} (Ω^{-1} m^{-1} s^{-1}). By changing the temperature, we could significantly analyze the difference in electrical conductivity as demonstrated in Fig. 13 (d).

4 Conclusion

The focus of present research is to investigate the physical characteristics and stability of RhZrX (X = P, As, Sb, Bi) HH alloys using theoretical methods. For this we utilized the full potential linearized augmented plane-wave (FP-LAPW) method in the framework of density functional theory (DFT). Our results indicate that these alloys exhibit positive frequency and brittle nature, ensuring their dynamic and mechanical stability. We also found that these alloys possess semiconductor characteristics with an indirect band gap of 1.50 eV, 1.47 eV, 1.38 eV, and 1.18 eV, as per electronic band structure calculations. Furthermore, we used the semi-classical Boltzmann method to examine the Seebeck coefficient, electrical conductivity, thermal conductivity, power factor and Fig. of merit as functions of temperature and chemical potential. Our calculation includes the effect of temperature on relaxation time, which is not commonly considered in theoretical studies. τ value is assumed to be a constant, and its typical value is around 10^{-14} *s*. Respective estimated values of Seebeck coefficient of 239, 231, 235 and 236 μV/K suggest p-type character. The calculated values of ZT for RhZrX (X = P, Sb, Bi) are not very high at room temperature but at high temperature these values are noticeable viz 0.4, 0.7, 0.38 and 0.37, respectively. The significant intensity of the absorption coefficient that is calculated for energies above 3 eV indicates that the compounds under investigation have the ability to absorb both visible and ultraviolet light. Our findings support the potential of RhZrX for thermoelectric and optoelectronic applications.

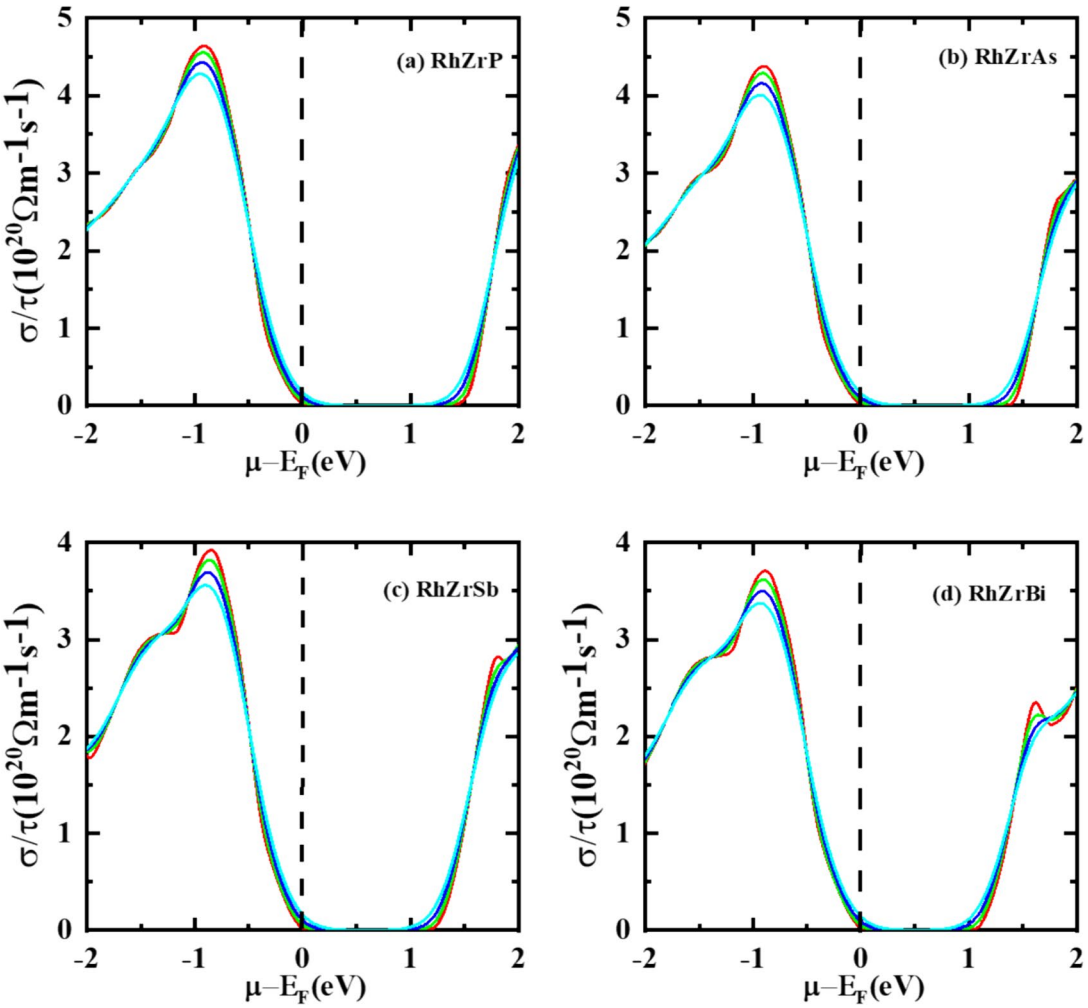

Fig. 13 The calculated electrical conductivity per relaxation time (σ/τ) of **a** RhZrP **b** RhZrAs **c** RhZrSb **d** RhZrBi HH alloys against chemical potential (μ-E_f)

Acknowledgements The authors extend their appreciation to Researchers Supporting Project number (RSPD2024R965), King Saud University, Riyadh, Saudi Arabia.

Author Contribution Mumtaz Manzoor, Arti Saxena, Pramod Kumar Singh, Faizan Ahmed- Conceptualization, Methodology, Investigation, formal analysis, Software, Writing- Original draft preparation Ramesh Sharma, Hamidullah, Dalia Fouad, Vipul Srivastava-Writing- Original draft preparation, Visualization, Investigation. Writing- Reviewing and Editing.

Funding The authors extend their appreciation to Researchers Supporting Project number (RSPD2024R965), King Saud University, Riyadh, Saudi Arabia.

Data Availability No datasets were generated or analysed during the current study.

Declarations

Competing of interests The authors declare no competing interests.

References

1. S. Muhammad Khuram et al., First-principles calculations to investigate structural, electronic, elastic and optical properties of radium based cubic fluoro-perovskite materials. Heliyon **9**(2), e13687 (2023)
2. T. Arakawa, H. Kurachi, J. Shiokawa, Physicochemical properties of rare earth perovskite oxides used as gas sensor material. J. Mater. Sci. **20**, 1207–1210 (1985)
3. A.A. Bokov, Z.-G. Ye, Recent progress in relaxor ferroelectrics with perovskite structure. J. Mater. Sci. **41**, 31–52 (2006)

4. C. Israel, M.J. Calderon, N.D. Mathur, The current spin on manganites. Mater. Today **10**(10), 24–32 (2007)
5. C.H. Kim et al., Strontium-doped perovskites rival platinum catalysts for treating NO x in simulated diesel exhaust. Science **327**(5973), 1624–1627 (2010)
6. N.D. Mathur et al., Large low-field magnetoresistance in La0. 7Ca0. 3MnO3 induced by artificial grain boundaries. Nature **387**(6630), 266–268 (1997)
7. M. Oudah et al., Superconductivity in the antiperovskite Dirac-metal oxide Sr3− x SnO. Nat. Commun. **7**(1), 13617 (2016)
8. J. Nuss et al., Tilting structures in inverse perovskites, M3Tto (M= ca, sr, ba, eu; Tt= si, ge, sn, pb) Acta Crystallographica Section B: Structural Science. Cryst. Eng. Mater. **71**(3), 300–312 (2015)
9. T. Kariyado, M. Ogata, Three-dimensional Dirac electrons at the Fermi energy in cubic inverse perovskites: Ca3PbO and its family. J. Phys. Soc. Jpn. **80**(8), 083704 (2011)
10. M. Bilal, S. Jalali-Asadabadi, R. Ahmad, I. Ahmad, Electronic properties of antiperovskite materials from state-of-the-art density functional theory. J. Chem. **2015**, 495131 (2015)
11. N. Iram, R. Sharma, J. Ahmad, M.M. Al-Anazy, E.S. Yousef, Z. Ahmad, First-principles investigation on anti-perovskites on Rb_3OX (X=Cl, Br, I): promising compounds for high performance photovoltaics and thermoelectric. Mater. Sci. Semicond. Process. **174**, 108168 (2024)
12. M. Bilal, B. Khan, H.R. Aliabad, M. Maqbool, S.J. Asadabadi, I. Ahmad, Thermoelectric properties of SbNCa3 and BiNCa3 for thermoelectric devices and alternative energy applications. Comput. Phys. Commun. **185**(5), 1394–1398 (2014)
13. R.J. Quinn, J.-W. Bos, Advances in half-Heusler alloys for thermoelectric power generation. Mater. Adv. **2**(19), 6246–6266 (2021)
14. M. Hichour, R. Khenata, D. Rached, M. Hachemaoui, A. Bouhemadou, A.H. Reshak, F. Semari, FP-APW+ lo study of the elastic, electronic and optical properties for the cubic antiperovskite ANSr3 (A= As, Sb and Bi) under pressure effect. Physica B **405**(7), 1894–1900 (2010)
15. T. Zhu, Fu. Chenguang, H. Xie, Y. Liu, X. Zhao, High efficiency half-Heusler thermoelectric materials for energy harvesting. Adv. Energy Mater. **5**(19), 1500588 (2015)
16. D. Cherrad, M. Maouche, M. Maamache, L. Krache, Influence of valence electron concentration on elastic, electronic and optical properties of the alkaline-earth tin oxides A3SnO (A= Ca, Sr and Ba): A comparative study with ASnO3 compounds. Phys. B: Cond. Matter **406**(14), 2714–2722 (2011)
17. D. Samal, H. Nakamura, H. Takagi, Molecular beam epitaxy of three-dimensional Dirac material Sr_3PbO. APL Mater. **4**(7), 076101 (2016)
18. T.H. Hsieh, J. Liu, Fu. Liang, Topological crystalline insulators and Dirac octets in antiperovskites. Phys. Rev. B **90**(8), 081112 (2014)
19. Y. Okamoto, A. Sakamaki, K. Takenaka, Thermoelectric properties of antiperovskite calcium oxides Ca_3PbO and Ca_3SnO. J. Appl. Phys. **119**(20), 205106 (2016)
20. W. Hsin, S. Bai. (2021) "Measurement techniques of thermoelectric devices and modules," Thermoelectric Energy Conversion, Woodhead Publishing, 521–537
21. D.M. Rowe (ed.), *Materials, preparation, and characterization in thermoelectrics* (CRC Press, Boca Raton, 2017)
22. W. Liu, Q. Jie, H.S. Kim, Z. Ren, Current progress and future challenges in thermoelectric power generation: from materials to devices. Acta Mater. **87**, 357–376 (2015)
23. D. Champier, Thermoelectric generators: a review of applications. Energy Convers. Manage. **140**, 167–181 (2017)
24. Jones, Christopher David Wilson. Synthesis, structure and properties of potential thermoelectric materials. Cornell University, 1999.
25. X.-L. Shi, J. Zou, Z.-G. Chen, Advanced thermoelectric design: from materials and structures to devices. Chem. Rev. **120**(15), 7399–7515 (2020)
26. T. Zhu, Y. Liu, Fu. Chenguang, J.P. Heremans, J.G. Snyder, X. Zhao, Compromise and synergy in high-efficiency thermoelectric materials. Adv. Mater. **29**(14), 1605884 (2017)
27. G.J. Snyder, E.S. Toberer, Complex thermoelectric materials. Nat. Mater. **7**(2), 105–114 (2008)
28. M.W. Gaultois, T.D. Sparks, C.K.H. Borg, R. Seshadri, W.D. Bonificio, D.R. Clarke, Data-driven review of thermoelectric materials: performance and resource considerations. Chem. Mater. **25**(15), 2911–2920 (2013)
29. K. Xia, H. Chaoliang, F. Chenguang, Z. Xinbing, Z. Tiejun, Half-Heusler thermoelectric materials. Appl. Phys. Lett. **118**(14), 140503 (2021)
30. R. Saravanan, Charge density and structural characterization of thermoelectric materials. Materials Research Forum LLC (2016). p. 184
31. S.A. Khandy, J.D. Chai, Strain engineering of electronic structure, phonon, and thermoelectric properties of p-type half-heusler semiconductor. J. Alloy. Compd. **850**, 156615 (2021)
32. S. Chen, Z. Ren, Recent progress of half-Heusler for moderate temperature thermoelectric applications. Mater. Today **16**(10), 387–395 (2013)
33. S.A. Khandy, K. Kaur, S. Dhiman, J. Singh, V. Kumar, Exploring thermoelectric properties and stability of half-Heusler PtXSn (X= Zr, Hf) semiconductors: a first principle investigation. Comput. Mater. Sci. **188**, 110232 (2021)
34. A. Amudhavalli, R. Rajeswarapalanichamy, K. Iyakutti, Half metallic ferromagnetism in Ni based half Heusler alloys. Comput. Mater. Sci. **148**, 87–103 (2018)
35. P. Kumari, R. Sharma, U. Lilhore, R. Khenata, V. Srivastava, First-principles study on structural, electronic, elastic, mechanical, thermodynamic, and thermoelectric properties of RbSnX3 (X= F, Cl, and Br) perovskites. Int. J. Energy Res. **46**(15), 23893–23907 (2022)
36. A.A. Musari, Electronic, mechanical, vibrational and thermodynamic properties of FeXSb (X= Hf and Nb) Half-Heusler alloys from first-principles approach. Solid State Sci. **122**, 106755 (2021)
37. E.K. Dogan, S.E. Gulebaglan, Some properties of LiInSi half-Heusler alloy via density functional theory. Bull. Mater. Sci. **44**(3), 208 (2021)
38. R. Paudel, G.C. Kaphle, M. Batouche, J. Zhu, Half-metallicity, magnetism, mechanical, thermal, and phonon properties of FeCrTe and FeCrSe half-Heusler alloys under pressure. Int. J. Quantum Chem. **120**(24), e26417 (2020)
39. D.I. Kars, O.C. Yasemin, First-principles calculations of vibrational and optical properties of half-Heusler NaScSi. Indian J. Phys. **95**, 2303–2312 (2021)
40. C. Wu, W. Zheng, N. Si, W.J. Feng, F.G. Zhang, W. Jiang, The structural, half-metal, magnetic, and mechanical properties of full Heusler alloy CrCoVSb: a first-principles study. Chin. J. Phys. **66**, 436–443 (2020)
41. S. Singh, Assessing the thermoelectric properties of ScRhTe half-heusler compound. Comput. Cond. Matter **13**, 120–126 (2017)
42. D. Kalita, M. Ram, N. Limbu, R. Kalita, A. Saxena, Prediction of some physical properties in new half Heusler alloy NbAgSi. J. Solid State Chem. **310**, 122999 (2022)
43. T. Zerrouki, H. Rached, D. Rached, M. Caid, O. Cheref, M. Rabah, First-principles calculations to investigate structural stabilities, mechanical and optoelectronic properties of NbCoSn and NbFeSb half-Heusler compounds. Int. J. Quantum Chem. **121**(8), e26582 (2021)
44. Y. Rached, M. Caid, H. Rached, M. Merabet, S. Benalia, S. Al-Qaisi, D. Rached, Theoretical insight into the stability,

magneto-electronic and thermoelectric properties of XCrSb (X: Fe, Ni) half-Heusler alloys and their superlattices. J. Supercond. Novel Magn. **35**(3), 875–887 (2022)
45. Y. Rached, D. Rached, H. Rached, O. Cheref, M. Caid, M. Merabet, S. Benalia, I. Bourachid, L. Djoudi, DFT assessment on stabilities, electronic and thermal transport properties of CoZrSb1− x Bi x half-Heusler alloys and their superlattices. The Eur. Phys. J. Plus **138**(4), 307 (2023)
46. F. Benzoudji, O.M. Abid, T. Seddik, A. Yakoubi, R. Khenata, H. Meradji, G. Uğur, S. Uğur, H.Y. Ocak, Insight into the structural, elastic, electronic, thermoelectric, thermodynamic and optical properties of MRhSb (M= Ti, Zr, Hf) half-Heuslers from ab initio calculations. Chinese J. Phys. **59**, 434–448 (2019)
47. L. Malsoon, P.P. Ferdinand, S.D. Mahanti, Electronic structure and thermoelectric properties of Sb-based semiconducting half-Heusler compounds. Phys. Review B—Cond. Matter Mater. Phys.. **83**(8), 085204 (2011)
48. B. Anissa, D. Radouan, I. Kars Durukan, Study of structural, electronic, elastic, optical and thermoelectric properties of half-Heusler compound RbScSn: A TB-mBJ DFT study. Opt. Quantum Electr. **54**(6), 372 (2022)
49. İK. Durukan, Y.O. Ciftci, H. Tekin, A new candidate for optoelectronic device applications: CoTiX (X: P, As, Sb) half-heusler compounds. Phys. B: Cond. Matter **678**, 415752 (2024)
50. M. Abubakr, K. Fatima, Z. Abbas, I. Gorczyca, M. Irfan, S. Muhammad, M.A. Khan, S.S. Alarfaji, Study of structural, optoelectronic and magnetic properties of Half-Heusler compounds QEuPa (Q= Ba, be, Mg, Sr) using first-principles method. J. Solid State Chem. **304**, 122612 (2021)
51. A. Nazir, E.A. Khera, M. Manzoor, B.A. Al-Asbahi, R. Sharma, Tunable opto-electronic and thermoelectric response of alkali based half-Heusler semiconductors AMgN (A= Rb, Cs) for sustainable energy: a computational approach. Mater. Sci. Eng. B **303**, 117338 (2024)
52. N. Mehmood, R. Ahmad, Structural, electronic, magnetic, and optical properties of half-Heusler alloys RuMnZ (Z= P, As): a first-principle study. J. Supercond. Novel Magn. **31**, 233–239 (2018)
53. R. Ahmad, N. Mehmood, S. Bukhari, W. Nafees, M. Arif, Ab initio study of half-Heusler compounds MnVZ (Z= P, As, Sb). J. Supercond. Novel Magn. **31**, 2617–2627 (2018)
54. B.S. Ahmed, B. Anissa, D. Radouan, N.A. Bouzieh, I. Kars Durukan, N. Amrane, DFT studies on electronic, elastic, thermoelectric and optical properties of new half-heusler XRhZ (X= V, Nb and Z= Si, Ge) semiconductors. East Eur. Opean J. Phys. **1**, 294–307 (2024)
55. B. Anissa, D. Radouan, B. Benaouda, Optical and thermoelectric response of RhTiSb half-Heusler. Int. J. Modern Phys. B **33**(22), 1950247 (2019)
56. Y.S. Kim, M. Marsman, G. Kresse, F. Tran, P. Blaha, Towards efficient band structure and effective mass calculations for III-V direct band-gap semiconductors.". Phys. Rev. B—Cond. Matter Mater. Phys. **82**(20), 205212 (2010)
57. M. Ameri, A. Touia, R. Khenata, Y. Al-Douri, H. Baltache, Structural and optoelectronic properties of NiTiX and CoVX (X= Sb and Sn) half-Heusler compounds: an ab initio study. Optik **124**(7), 570–574 (2013)
58. R. Ahmed, N.S. Masuri, B.U. Haq, A. Shaari, S. AlFaifi, F.K. Butt, M.N. Muhamad, M. Ahmed, S.A. Tahir, Investigations of electronic and thermoelectric properties of half-Heusler alloys XMgN (X= Li, Na, K) by first-principles calculations. Mater. Des. **136**, 196–203 (2017)
59. M.J. Winiarski, K. Bilińska, High thermoelectric power factors of p-type half-Heusler alloys YNiSb, LuNiSb, YPdSb, and LuPdSb. Intermetallics **108**, 55–60 (2019)
60. A. Touia, K. Benyahia, A. Tekin, First-principles calculations of structural, electronic, optical, and thermoelectric properties of LuNiBi and LuNiSb half-heusler. J. Supercond. Novel Magn. **34**(10), 2689–2698 (2021)
61. B. Anissa, D. Radouan, B. Benaouda, A. Omar, First-principles study of structural, electronic, thermodynamic, and thermoelectric properties of a new ternary half-Heusler alloy PdZrGe. Chin. J. Phys. **56**(6), 2926–2936 (2018)
62. P.O. Adebambo, G.A. Adebayo, R. Guerra, D. Ceresoli, Electronic and phonon contributions to the Thermoelectric properties of newly discovered half-Heusler alloy s XHfPb (X= Ni, Pd, and Pt). J. Phys. Chem. Solids **174**, 111196 (2023)
63. D. Radouan, B. Anissa, B. Benaouda, Investigation of electronic, optical, and thermoelectric properties of new d0 half-metallic half-Heusler alloys SiLiX (X= Ca and Sr). Emergent Materials **5**(4), 1097–1108 (2022)
64. L. Shao, X. Zhang, Y. Chen, L. Zhu, S. Wu, Q. Liu, T. Wang, Why do cracks occur in the weld joint of Ti-22Al-25Nb alloy during post-weld heat treatment? Front. Mater. **10**, 1135407 (2023)
65. Z. Zhang, J. Chen, J. Wang, Y. Han, Z. Yu, Q. Wang, S. Yang, Effects of solder thickness on interface behavior and nanoindentation characteristics in Cu/Sn/Cu microbumps. Welding World **66**(5), 973–983 (2022)
66. J. Zhang, L. Wang, A. Zhong, G. Huang, F. Wu, D. Li, D. Han, Deep red PhOLED from dimeric salophen platinum (II) complexes. Dyes Pigments **162**, 590–598 (2019)
67. J. Zhang, A. Zhong, G. Huang, M. Yang, D. Li, M. Teng, D. Han, Enhanced efficiency with CDCA co-adsorption for dye-sensitized solar cells based on metallosalophen complexes. Sol. Energy **209**, 316–324 (2020)
68. C. Zhu, M. Aldossari, S. Rezapour, S. Shateyi, B. Gunay, Analytical optical solutions to the nonlinear Zakharov system via logarithmic transformation. Results Phys. **56**, 107298 (2024)
69. H. Zaari, A.G. El Hachimi, A. Benyoussef, A. El Kenz, Comparative study between TB-mBJ and GGA+ U on magnetic and optical properties of CdFe2O4. J. Magn. Magn. Mater. **393**, 183–187 (2015)
70. V.L. Lignères, E.A. Carter, "An introduction to orbital-free density functional theory, in *Handbook of materials modeling: methods*. (Springer, Netherlands, Dordrecht, 2005), pp.137–148
71. J. Yang, G.P. Meisner, L. Chen, Strain field fluctuation effects on lattice thermal conductivity of ZrNiSn-based thermoelectric compounds. Appl. Phys. Lett. **85**(7), 1140–1142 (2004)
72. J.P. Perdew, K. Burke, M. Ernzerhof, Generalized gradient approximation made simple. Phys. Rev. Lett. **77**(18), 3865 (1996)
73. C. Stampfl, C.H.G. Van de Walle, Density-functional calculations for III-V nitrides using the local-density approximation and the generalized gradient approximation. Phys. Rev. B **59**(8), 5521 (1999)
74. A.D. Becke, R.J. Erin, A simple effective potential for exchange. J. Chem. Phys. **124**(22), 221101 (2006)
75. M. Hassan et al., Investigation of ferromagnetic semiconducting and opto-electronic properties of Zn1− xMnxS (0≤ x≤ 1) alloys: A DFT-mBJ approach. Curr. Appl. Phys. **16**(11), 1473–1483 (2016)
76. A. Bouhemadou, Prediction study of structural and elastic properties under pressure effect of M2SnC (M= Ti, Zr, Nb, Hf). Phys. B: Cond. Matter **403**(17), 2707–2713 (2008)
77. T. Wu, J. Wan, L. Xiaoya, Z. Yanfei, C. Lidong, Thermoelectric properties of p-type Fe-doped TiCoSb half-Heusler compounds. J. Appl. Phys. **102**(10), 103705 (2007)
78. A. Bouhemadou, R. Khenata, F. Zerarga, Prediction study of structural and elastic properties under pressure effect of CdX2O4

(X= Al, Ga, In) spinel oxides. Comput. Mater. Sci. **39**(3), 709–712 (2007)
79. Yu. Xia, S. Bhattacharya, V. Ponnambalam, A.L. Pope, S.J. Poon, T.M. Tritt, Thermoelectric properties of semimetallic (Zr, Hf) CoSb half-Heusler phases. J. Appl. Phys. **88**(4), 1952–1955 (2000)
80. J. Toboła, J. Pierre, Electronic phase diagram of the XTZ (X= Fe Co, Ni; T= Ti, V, Zr, Nb, Mn; Z= Sn, Sb) semi-Heusler compounds. J. Alloy. Compd. **296**(1–2), 243–252 (2000)
81. P. Blaha, K. Schwarz, G.K.H. Madsen, D. Kvasnicka, J. Luitz, R. Laskowski, F. Tran, L.D. Marks, *WIEN2k: An Augmented Plane Wave Plus Local Orbitals Program for Calculating Crystal Properties* (Vienna University of Technology, Austria, 2018)
82. G.K.H. Madsen, D.J. Singh, BoltzTraP. A code for calculating band-structure dependent quantities. Comput. Phys. Commun. **175**(1), 67–71 (2006)
83. V. Srivastava, N. Kaur, X. Wang, M. Mushtaq, S.A. Dar, First-principles study on structural, electronic, magnetic, elastic, mechanical and thermodynamic properties of Mn2PtCo Heusler alloy. Int. J. Energy Res. **45**(7), 11305–11319 (2021)
84. The Materials Project: a materials genome approach to accelerating materials innovation. https://next-gen.materialsproject.org/materials/mp-961720?formula=ZrAsRh#crystal_structure
85. Z. Wu, X.-J. Chen, V.V. Struzhkin, R.E. Cohen, Trends in elasticity and electronic structure of transition-metal nitrides and carbides from first principles. Phys. Rev. B **71**(21), 214103 (2005)
86. C. Ambrosch-Draxl, J.O. Sofo, Linear optical properties of solids within the full-potential linearized augmented planewave method. Comput. Phys. Commun. **175**(1), 1–14 (2006)
87. A. Settouf, H. Rached, N. Benkhettou, D. Rached, DFT calculations of structural, optoelectronic and thermodynamic properties of BxAl1-xP alloys. Comput. Cond. Matter **19**, e00377 (2019)
88. A. Benslimane, S. Kouidri, H. Rached, M. El Keurti, S. Meliani, M. Ould Moussa, Electronic structures and optical responses of Sb2S3, Ag2S, AgSbS2, and Ag3SbS3 compounds: an assessment of DFT calculations. Indian J. Phys. **98**(3), 955–966 (2024)
89. A. Jayaraj, I. Siloi, M. Fornari, M.B. Nardelli, Relaxation time approximations in PAOFLOW 20. Sci. Rep. **12**(1), 4993 (2022)
90. A. Bulusu, D.G. Walker, Review of electronic transport models for thermoelectric materials. Superlattices Microstruct. **44**(1), 1–36 (2008)
91. Y. Zhao, Y. Sun, H. Hou, Core-shell structure nanoprecipitates in Fe-xCu-3.0Mn-1.5Ni-1.5Al alloys: a phase field study. Progress Nat. Sci.: Mater. Int. **32**(3), 358–368 (2022)
92. X. Xu, Y. Hao, R. Dong, H. Hou, Y. Zhao, Effect of undercooling on microstructure evolution of Cu based alloys. J. Alloy. Compd. **935**, 167998 (2023)